Double photoelectron momentum spectra of helium at infrared wavelength

Alejandro Zielinski, Vinay Pramod Majety, and Armin Scrinzi
Physics Department, Ludwig Maximilians Universität, D-80333 Munich, Germany
(Received 24 November 2015; published 8 February 2016)

Double photoelectron momentum spectra of the helium atom are calculated *ab initio* at extreme ultraviolet and near-infrared wavelengths. At short wavelengths two-photon double-ionization yields, two-electron energy spectra, and triply differential cross sections agree with results from recent literature. At the near-infrared wavelength of 780 nm the experimental single-to-double-ionization ratio is reproduced up to intensities of 4×10^{14} W/cm^2, and two-electron energy spectra and joint angular distributions are presented. The time-dependent surface flux approach is extended to full $3 + 3$ spatial dimensions and systematic error control is demonstrated. We analyze our differential spectra in terms of an experimentally accessible quantitative measure of correlation.

DOI: 10.1103/PhysRevA.93.023406

I. INTRODUCTION

Understanding the quantum dynamics of the three-body Coulomb problem is a fundamental and ongoing challenge. As one of its most elementary realizations, the three-body breakup of helium atoms by short and intense laser pulses has been examined extensively over the past few decades. The dynamics and correlation in this simple process provide an important model for understanding more complex few-body phenomena.

A multitude of mechanisms for the ionization of He have been identified in the various intensity and wavelength regimes. For example, at long laser wavelengths in the near infrared (IR) and at high intensities, double ionization (DI) is well described by two independent tunnel ionization events. At lower intensities, however, the DI yield predicted by such a model is far too small. The observed enhancement of the DI yield by several orders of magnitude compared to the expectation for a sequence of two independent processes appears not just in helium [1] but in many atoms and molecules [2]. To explain the discrepancy, various so-called nonsequential double-ionization (NSDI) mechanisms have been proposed (an overview can be found in, e.g., [3]). The NSDI models are all based on the recollision scenario of the "three-step model" [4], where one electron escapes via tunnel ionization, picks up energy from the laser field, and is redirected back on the ion when the field reverses its direction. Upon recollision the first electron can interact with the second electron and the nucleus in various ways. It may directly dislodge the second electron, leading to simultaneous ejection (SE) of both electrons, also called the direct pathway. It may also lift the second electron to an excited state from which the field can ionize it on its own, also called recollision-induced excitation with subsequent ionization (RESI), which can result in a delayed pathway for the second electron that leads to emission into opposite directions [5,6]. The first electron can also form a bound compound with the second electron and the nucleus which survives for at least a quarter of a cycle (doubly delayed ejection, DDE) [7], a process which can also occur when the kinetic energy of the recolliding electron is smaller than the excitation energy of the ion. Details and the interplay of all these mechanisms are not yet fully understood, and require testing against accurate benchmark data.

Another process that has received significant attention is two-photon DI of the He atom. This occurs in the extreme ultraviolet (XUV) when the energy of two photons suffices for DI and it dominates up to the threshold for single-photon DI. The process necessarily probes correlation dynamics, most simply by shake-up into an excited ionic state during detachment of the first electron, followed by second ionization of the excited ionic state. Also, more direct processes were considered that involve correlated initial and final states; see, e.g., [8]. In numerical simulations, consensus appears to be arising in recent literature for photon energies $\omega \approx 40$–54 eV; see, e.g., [9].

At present, the most complete experimental tests for the mechanisms discussed above are provided by detecting, in coincidence, the momenta of two particles from the fully fragmented state consisting of the two ionized electrons and the remaining ion. Momentum imaging techniques like COLTRIMS (cold target recoil-ion momentum spectroscopy) [10] and continued advances in laser technologies have opened up the possibility to study the correlated three-particle Coulomb breakup in helium experimentally on its intrinsic time scale; see, for example, [11–15]. Due to the high binding energies of the helium atom and the resulting low efficiency of laser-induced ionization, many DI experiments are performed with other targets, such as neon [15] or argon atoms [16–20]. Final-state correlations are one of the more accessible observables, but also more convoluted questions are being investigated, like the exact release time of the electrons [17]. Although experimentally more challenging, data for helium is often preferable as the additional electrons in multielectron targets complicate analysis and model building.

Apart from the discussion of simplifying models, significant effort has been invested into numerical computations. The main goal is to obtain reliable benchmark data that are not obscured by experimental limitations. Advances in numerical techniques and ever-increasing computational resources allowed for extensive *ab initio* calculations of the helium system.

At short laser wavelengths, where dynamics are initiated by the absorption of only few photons, fully differential photoelectron spectra and cross sections have been computed using a wide array of methods. As laser-atom interaction at XUV wavelength is weak, time-independent perturbative methods can be applied [21,22]. For such approaches, representation of

the double continuum is the major computational task, for which a variety of techniques exist; see, for example, the discussions in Refs. [23,24]. Two-photon double ionization has also been successfully calculated using R-matrix Floquet theory [25,26]. A large number of calculations resorted to numerical solutions of the time-dependent Schrödinger equation (TDSE) in full dimensionality; see, for example, [9,24,27–32].

At longer wavelengths such computations remain challenging. The reason is the inapplicability of perturbative approaches, which only allows for time-dependent nonperturbative methods relying on numerical solutions of the TDSE. Unfortunately, calculations are subjected to a rather unfavorable scaling of the problem size with the wavelength λ of the laser pulse proportional to λ^p, with $p \gtrsim 7$ (see Sec. II A) As a consequence, already at wavelengths $\lambda \sim 400$ nm full dimensional numerical computations are scarce [33–35]. Progress at longer wavelengths like the experimentally relevant Ti:sapphire wavelength of 780 nm has only been made recently. Weak IR dressing fields, unable to ionize on their own, were combined with XUV pulses in Ref. [32] to study their effect on joint angular distributions for coplanar emission. In Ref. [36] a study of the enhancement of double emission by an XUV pulse in the presence of a moderately intense single-cycle IR pulse required more than 4000 cores of a supercomputer for computation. In Ref. [33], at very high computational expense, ionization due to a pure 780-nm IR pulse could be computed, but no spectra were given.

In this article, we present accurate *ab initio* DI spectra at both XUV and IR wavelengths. In the XUV regime, we reproduce results from literature and corroborate the consensus that has emerged in recent publications for observables such as the total DI cross section, two-electron energy distributions, and triply differential cross sections. Compared to literature, we were able to significantly reduce the computational effort.

At the near-IR wavelength of 780 nm, we present differential spectra for intensities up to 4×10^{14} W/cm^2 and pulse durations $\gtrsim$10 fs. The measured single-to-double-ionization ratio—the IR DI "knee"—is reproduced. We further present two-electron energy distributions and up to fivefold differential momentum spectra.

Throughout, convergence is studied systematically and provides error estimates from below 5% in the XUV regime to $\lesssim$30% for a large part of the IR data. At certain energies errors of threefold differential spectra are beyond these values and the fivefold differential spectra at IR wavelength must be considered only as qualitative results, as convergence could not yet be achieved. For quantitative analysis we suggest a measure of correlation that is directly applicable to experimental double-emission spectra.

All calculations are based on an extension of the time-dependent surface flux (tSurff) method to the six-dimensional double-emission problem. The three-dimensional single-particle version of the method [37] has been applied to several systems [38–43]. A first formulation for double emission from a $1+1$-dimensional model system was given in Ref. [44]. Here we give the $3+3$-dimensional version of tSurff that is needed for DI in realistic systems.

The paper is organized as follows. In the next section we specify the problem and summarize the general approach. Then we describe the tSurff method for double emission followed by a discussion of the method's limitations and error control. In Sec. III we present details of the implementation. Then we compare our results with various previous theoretical and experimental publications at XUV wavelengths to verify the validity of the method. Finally, we present our results for fully differential DI spectra in the IR regime in Sec. VI. Technical details of the method are presented in several Appendixes.

II. TSURFF FOR DOUBLE PHOTOEMISSION

A. Direct computation of double emission

A helium atom interacting with an external electric field is described by the Hamilton operator

$$H(t) = H_{\rm ion}(t) \otimes \mathbb{1} + \mathbb{1} \otimes H_{\rm ion}(t) + \frac{1}{|\vec{r}_1 - \vec{r}_2|}, \qquad (1)$$

where

$$H_{\rm ion}(t) = -\frac{\Delta}{2} - i\,\vec{A}(t)\cdot\vec{\nabla} - \frac{2}{r} \qquad (2)$$

is the single-electron Hamiltonian of the ionic problem and $\mathbb{1}$ is the identity operator. Atomic units ($\hbar = m_e = e^2 = 4\pi\epsilon_0 \equiv 1$) are used unless indicated otherwise. The motion of the nucleus is neglected. For the interaction with the field $\vec{\mathcal{E}}(t) = -\partial_t \vec{A}(t)$ we employ the dipole approximation, which is appropriate down to wavelengths in the XUV ($\gtrsim$10 nm). The reasons for choosing the velocity gauge form of the dipole interaction are detailed in Sec. III C.

Here we discuss only linear polarization and choose the z axis to coincide with the laser polarization direction. One reason for this choice is that the recollision mechanism largely responsible for DI is most effective for linear polarization. A more mundane reason is that cylindrical symmetry reduces the spatial dimensions to five instead of six for general polarization.

The goal is to extract both single- and double-ionization photoelectron spectra generated by an external laser pulse from the solution of the TDSE,

$$i\frac{d}{dt}\Psi(t) = H(t)\Psi(t), \qquad (3)$$

starting from the ground state.

The direct approach to this problem consists of two steps, both of which are numerically challenging. First, the multichannel wave function Ψ including double continuum contributions needs to be computed at the end of the pulse, a task whose complexity depends on the laser parameters. In particular, it scales very unfavorably with the laser wavelength due to a simultaneous expansion in momentum, space, and time. At high intensities I and long wavelengths λ, the peak electron momenta are dominated by the vector potential $A \propto \lambda\sqrt{I}$. For correctly representing such momenta, thinking in terms of grids, the grid point density must be increased in proportion to the maximal momentum $p_{\rm max}$. The increase of both $p_{\rm max} \propto \lambda\sqrt{I}$ and pulse duration $\propto\lambda$ let the spatial extension of the solution grow to a maximal radius $R_{\rm max} \propto \lambda^2\sqrt{I}$. As a result, the required number of discretization points in the laser direction grows as $\propto\lambda^3 I$. Any discretization, not only grids, is subjected to the same general scaling. Considering

only the growth of the radial discretization of the two electrons and assuming pulse durations $\propto\lambda$, the computational effort for solving a two-electron system grows as $\propto\lambda^7 I^2$. This is a conservative estimate as it ignores the effects on the angular degrees of freedom and on the time step size.

The second difficulty arises in the analysis of the wave function Ψ after the end of the pulse. For extracting the double-emission amplitudes, one would need to know the two-particle stationary scattering solutions $\chi_{\vec{k}_1,\vec{k}_2}(\vec{r}_1,\vec{r}_2)$ for asymptotic outgoing single-particle momenta $\vec{k}_1$ and $\vec{k}_2$. Such solutions are not available and analysis involves additional hard-to-control approximations. A strategy for bypassing this problem is to propagate Ψ to sufficiently long times after the end of the pulse and then extract the relevant dynamical information entirely from the asymptotic region where effects of electron repulsion are disregarded. In this approximation, the scattering solutions are products of single-particle scattering wave functions $\chi_{\vec{k}_1,\vec{k}_2}(\vec{r}_1,\vec{r}_2) \approx \chi_{\vec{k}_1}(\vec{r}_1)\chi_{\vec{k}_2}(\vec{r}_2)$, where popular choices for $\chi_{\vec{k}_i}$ are Coulomb or plane waves. The effect of this approximation can be controlled by propagating further into the asymptotic region. Various other strategies for the analysis of the multichannel wave function have been proposed, which all incur some form of inconvenience, ranging from large computational costs to the inability to extract differential information. Discussions can be found in Refs. [23,24] and the references therein.

The direct approach has been implemented by several groups using various combinations of strategies to tackle both steps. A particularly convincing example is Ref. [9], where the time-dependent close-coupling (TDCC) scheme [45] was implemented in a finite-element discrete variable representation (FE-DVR) [46,47] to compute differential two-photon cross sections. Box sizes of up to 800 a.u. were used to propagate up to 21 fs after the XUV laser pulse in order for the projection onto products of energy-normalized Coulomb waves to be accurate. The same numerical methods were used by various other groups to study DI by few photons [30,31,48] and the effects of an assisting IR field [32]. In Ref. [29] spatial discretization was by B splines and analysis by projection onto products of uncorrelated numerical single-electron continuum states. In Ref. [28] further propagation after the end of the pulse was avoided. The wave packet was analyzed in terms of three-body scattering solutions that are obtained by exterior complex scaling. This implies the product form $\chi_{\vec{k}_1}\chi_{\vec{k}_2}$ only outside the simulation box, where for the parameters of [28] a box size of $\sim$130 a.u. was required. A strategy employing a finite differences discretization and extraction of DI spectra using masks was used to study DI processes at 390 nm [34]. In Ref. [35] the same method was used to analyze the relative importance of various DI pathways at this wavelength, which required box sizes of up to 1200 a.u. In Ref. [36] an XUV pulse was used to enhance photo absorption from a very short IR pulse of moderate intensity. The computations employed similar numerical techniques as [9] and were conducted on a grid with over 300 a.u. radial extension.

B. Double emission by tSurff

In the direct approach, a significant part of the computational effort goes into reproducing basically trivial dynamics: Far away from the nucleus and when the electrons are far apart, the only relevant interaction of the electrons is with the external electric field. That is the point which is exploited by the tSurff method. Numerical simulation is limited to the volume inside a "tSurff radius" R_c, where interactions between the charges are important. Beyond that, spectra can be reconstructed from analytically known solutions for an electron in a dipole field. The numerical solution is spatially terminated by placing an efficient absorber outside R_c.

The following sections convey the basic idea of tSurff and present all formulas needed for computing double-emission spectra in $3+3$ dimensions. For a more detailed discussion, the reader is referred to Refs. [37,44]. In separate sections we explain the gain of the method, its scaling compared to the direct approach, and the special case of single emission from two-electron systems.

1. *tSurff for a single-particle problem*

Single-electron spectral densities can be expressed through spectral amplitudes $b(\vec{k})$ as

$$P(\vec{k}) = |b(\vec{k})|^2. \tag{4}$$

The fundamental idea of scattering theory is that at sufficiently large times $t \geqslant T$ and sufficiently large distances $|\vec{r}| \geqslant R_c$ the time evolution of the system equals the free time evolution such that the spectral amplitudes at momentum $\vec{k}$ reaching a detector outside R_c can be computed as

$$b(\vec{k}) \approx (2\pi)^{-3/2} \int_{|\vec{r}|>R_c} d\vec{r}\, e^{-i\vec{k}\vec{r}}\Psi(\vec{r},T). \tag{5}$$

The approximate sign accounts for the fact that exponential tails of the bound states will extend to infinite distances $|\vec{r}| > R_c$ and that at any finite T some low-momentum content of $\Psi(\vec{r},T)$ will not have left the region $|\vec{r}| < R_c$. Both errors rapidly decrease with growing T and R_c.

The analysis of $\Psi(\vec{r},T)$ in terms of field-free scattering solutions is meaningful only in absence of any external field. For laser ionization we must choose T after the end of the laser pulse. As typical laser pulse durations are several hundred atomic units, $\Psi(\vec{r},T)$, in general, extends over large distances. The overwhelming part of this extension is brought about by essentially free motion at distances $|\vec{r}| > R_c$. In tSurff, this motion is not simulated numerically, but is inferred from analytically known solutions.

For the practical implementation of the idea, let $H(\vec{r},t)$ be the Hamiltonian of the system in the field and let $H_V(\vec{r},t)$ be a time-dependent Hamiltonian with

$$H(\vec{r},t) = H_V(\vec{r},t), \quad |\vec{r}| > R_c, \tag{6}$$

for which we know solutions with the desired asymptotic momenta $\vec{k}$,

$$i\frac{d}{dt}\chi_{\vec{k}}(\vec{r},t) = H_V(\vec{r},t)\chi_{\vec{k}}(\vec{r},t). \tag{7}$$

Here we have in mind the Hamiltonian of a free electron in a dipole field,

$$H_V = -\frac{\Delta}{2} - i\vec{A}(t)\cdot\vec{\nabla}, \tag{8}$$

with the Volkov solutions

$$\chi_{\vec{k}}(\vec{r},t) = (2\pi)^{-3/2} e^{i\vec{k}\vec{r}} e^{-i\Phi(\vec{k},t)} \tag{9}$$

and the Volkov phase $\Phi(\vec{k},t) = \int^t d\tau[\vec{k}^2/2 + \vec{k}\vec{A}(\tau)]$. Introducing the notation

$$\Theta(\vec{r}) := \begin{cases} 0 & \text{for } |\vec{r}| < R_c, \\ 1 & \text{else,} \end{cases} \tag{10}$$

we can write the spectral amplitude (5) for our photoemission problem as

$$b(\vec{k}) \approx \langle \chi_{\vec{k}}(T)|\Theta|\Psi(T)\rangle, \tag{11}$$

where we have dropped the Volkov phase factor $\exp[i\Phi(\vec{k},t)]$ at $t = T$. By taking the time derivative and integrating over time, we find

$$\langle \chi_{\vec{k}}(T)|\Theta|\Psi(T)\rangle = i\int_{-\infty}^{T} dt \langle \chi_{\vec{k}}(t)|H_V\Theta - \Theta H|\Psi(t)\rangle. \tag{12}$$

The lower integration boundary of $-\infty$ is to be understood as any time before the onset of the laser field. By Eq. (6) the difference of operators reduces to a commutator,

$$H_V\Theta - \Theta H = [H_V,\Theta] = \left[-\frac{\Delta}{2} - i\vec{A}(t)\cdot\vec{\nabla},\Theta\right], \tag{13}$$

which is a flux operator on the surface $|\vec{r}| = R_c$ with a time-dependent correction accounting for the action of the external field; see also Appendix A. For evaluating the tSurff integral (12), we no longer need to integrate over the long-range behavior of $\Psi(\vec{r},T)$. Instead, we have a time integral over the surface flux. The time-dependent correction in the surface flux operator accounts for the acceleration of the electron by the dipole field outside R_c and ensures that the flux is counted into the correct final momentum.

An important complication of this idea is caused by the long-range nature of the Coulomb potential. It is well known that for scattering potentials with Coulomb-like asymptotics $V(r) \sim 1/r$, standard scattering theory suffers from a divergent error in the scattering phases at any finite T and R_c. In time-independent scattering this can be remedied by replacing the plane wave in Eq. (5) with a scattering solution of the corresponding Coulomb problem. For tSurff this is not viable, as no analytical solutions are known, where both the laser and the asymptotic Coulomb field are taken into account.

We solve this problem pragmatically by using R_c as a convergence parameter, i.e., increasing it until further changes fall below a desired accuracy limit. In practice, this is achieved by multiplying the potentials by a function $f_{\alpha,\beta}(r) = 1$ for $r < \alpha$ and $=0$ for $r > \beta$. For the transition from α to β we employ a third-order polynomial such that the derivatives are continuous at α and β. We usually choose $\beta = R_c$.

When highly accurate results are needed, the strategy above becomes costly and defeats the original purpose of tSurff, i.e., to keep R_c small. For such situations, analytic corrections to the plane-wave solutions, such as the Eikonal-Volkov solutions introduced in Ref. [49], may be helpful.

2. *tSurff in* 3 + 3 *spatial dimensions*

The tSurff method was extended to two-particle emission in Ref. [44] for the example of two one-dimensional particles. The straightforward extension for two three-dimensional particles is given here.

The experimentally observed momentum distribution density is expressed by the two-electron spectral amplitudes as

$$P(\vec{k}_1,\vec{k}_2) = |b(\vec{k}_1,\vec{k}_2)|^2. \tag{14}$$

For the computation of the $b(\vec{k}_1,\vec{k}_2)$, we truncate the long-range tails of the nuclear Coulomb potentials as in the single-electron case. In three-body breakup there is the additional complication that motion never can be considered as free near $\vec{r}_1 = \vec{r}_2$, where the two electrons repel each other irrespective of their distance from the nucleus. This difficulty is characteristic for the asymptotics of many-body scattering. We avoid it by suppressing the repulsion for $r_1, r_2 \geqslant R_c \geqslant \beta$:

$$\frac{1}{|\vec{r}_1 - \vec{r}_2|} \mapsto \frac{f_{\alpha,\beta}(r_1) f_{\alpha,\beta}(r_2)}{|\vec{r}_1 - \vec{r}_2|}. \tag{15}$$

This kind of approximation is not specific to tSurff. Any asymptotic analysis where the two-particle scattering functions are approximated as a product of single-particle functions implies that interparticle interactions are neglected in the asymptotic region. This is the case for all direct methods discussed above. Here we make this approximation manifest by suppressing the electron repulsion outside R_c: Rather than having a built-in error in the asymptotic analysis, we make a consistent spectral analysis of the approximate system.

We would like to point out that the approximation may possibly be avoided in tSurff [44]: An exact solution for two electrons in a laser field can be given in relative and center-of-mass coordinates $(\vec{r}_1 + \vec{r}_2)/2, \vec{r}_1 - \vec{r}_2$, if nuclear potentials can be neglected. In practice, this involves rather complicated transformations of the surfaces which we have not attempted to implement.

We divide the space of the radial coordinates of the two electrons into four regions (Fig. 1): $B := [0,R_c] \times [0,R_c]$, $S := [R_c,\infty) \times [0,R_c]$, $\overline{S} := [0,R_c] \times [R_c,\infty)$, and $D := [R_c,\infty) \times [R_c,\infty)$. Analogous to the single-electron case, for large R_c and at large T, the wave functions in these regions approximately contain the bound, singly ionized, and doubly ionized parts of the wave function, respectively.

With this partitioning, similar as for a single particle, we obtain the double scattering amplitude by analyzing the solution in region D only,

$$b(\vec{k}_1,\vec{k}_2) \approx \langle\langle \chi_{\vec{k}_1}(T)\chi_{\vec{k}_2}(T)\big|\Theta_1\Theta_2|\Psi(T)\rangle\rangle, \tag{16}$$

with $\Theta_i := \Theta(\vec{r}_i)$, $i = 1,2$; see Eq. (10). The double brackets $\langle\langle\cdots\rangle\rangle$ emphasize that integration is over both spatial coordinates. The bra function is the product of two Volkov waves $\chi_{\vec{k}_i}(\vec{r}_i,T)$, $i = 1,2$, with the respective asymptotic momenta. As all interactions have been switched off beyond R_c, these are correct asymptotic solutions for the truncated problem: In region D the truncated Hamiltonian is

$$H(t)|_D = H_V(t) \otimes \mathbb{1} + \mathbb{1} \otimes H_V(t), \tag{17}$$

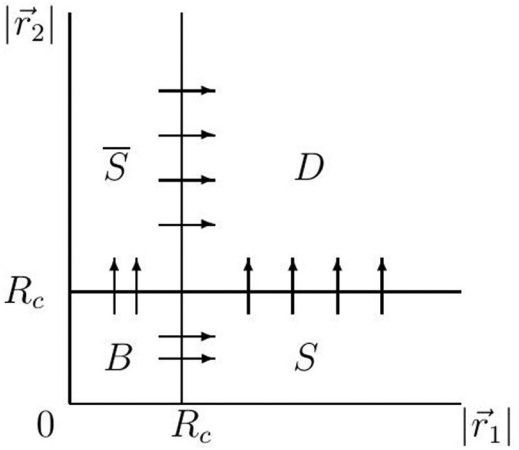

FIG. 1. Spatial partitioning of the wave function: At large times, regions B, S and $\overline{S}$, and D correspond to bound, singly ionized, and doubly ionized parts, respectively. Arrows symbolize the flux across the region boundaries.

with the Volkov Hamiltonian $H_V(t)$, Eq. (8), on the respective coordinates.

By similar steps as for a single particle, the spectral amplitude (16) can be evaluated as the time integral over fluxes F and $\overline{F}$ from regions S and $\overline{S}$ into D,

$$b(\vec{k}_1,\vec{k}_2,T) = \int_{-\infty}^{T} dt[\underbrace{F(\vec{k}_1,\vec{k}_2,t)}_{S\to D} + \underbrace{\overline{F}(\vec{k}_1,\vec{k}_2,t)}_{\overline{S}\to D}]. \tag{18}$$

By exchange symmetry, we have $F(\vec{k}_1,\vec{k}_2) = \overline{F}(\vec{k}_2,\vec{k}_1)$. Details of the derivation can be found in Ref. [44].

The flux F is determined by the time evolution on S, where the Hamiltonian is given by

$$H(t)|_S = H_V(t) \otimes \mathbb{1} + \mathbb{1} \otimes H_{\rm ion}(t), \tag{19}$$

with $H_{\rm ion}$ obtained from Eq. (2) by truncating the Coulomb tails. Solutions for $H(t)|_S$ can be written as the product of a Volkov wave $\chi_{\vec{k}_1}(\vec{r}_1,t)$ and the solution of an ionic problem $\varphi_{\vec{k}_1}(\vec{r}_2,t)$ on $|\vec{r}| < R_c$. With this the flux from S into D is given as

$$F(\vec{k}_1,\vec{k}_2,t) = \left\langle \chi_{\vec{k}_2}(t)\middle|[H_V,\Theta_2]\middle|\varphi_{\vec{k}_1}(t)\right\rangle, \tag{20}$$

where we again refer to [44] for the derivation. For details on the evaluation of F, see Appendix A.

It is important to note that the ionic factor $\varphi_{\vec{k}_1}(\vec{r}_2,t)$ for $\vec{r}_2$ depends on the asymptotic momentum $\vec{k}_1$ in the $\vec{r}_1$ direction. This coupling occurs, as $\varphi_{\vec{k}_1}$ is determined by an *inhomogeneous* TDSE, where the inhomogeneity accounts for the flux from region B into S; see Fig. 1. The flux $B \to S$ is correlated, such that each momentum component $\vec{k}_1$ contributes differently to the wave function in $\vec{r}_2$ direction. The inhomogeneous equation for $\varphi_{\vec{k}_1}(\vec{r}_2,t)$ is

$$i\frac{d}{dt}\varphi_{\vec{k}_1}(\vec{r}_2,t) = H_{\rm ion}(t)\varphi_{\vec{k}_1}(\vec{r}_2,t) - C_{\vec{k}_1}(\vec{r}_2,t), \tag{21}$$

with the source term

$$C_{\vec{k}_1}(\vec{r}_2,t) = \int d\vec{r}_1 \overline{\chi_{\vec{k}_1}(\vec{r}_1,t)}[H_V(\vec{r}_1),\Theta_1]\Psi(\vec{r}_1,\vec{r}_2,t) \tag{22}$$

and initial condition

$$\varphi_{\vec{k}_1}(\vec{r}_2,t=-\infty) = 0. \tag{23}$$

For evaluating (22) we need the values and derivatives of $\Psi(\vec{r}_1,\vec{r}_2,t)$ on the boundary $|\vec{r}_1| = R_c$ between domains B and S. This requires the solution of the full six-dimensional (in case of linearly polarized pulses five-dimensional) two-electron TDSE on B. Beyond R_c the two-particle wave function Ψ can be disposed of by absorption. Details on the choice of absorber and its implementation are given in Sec. III C.

3. *Procedure and computational gain*

In principle and in practice, the computation of the surface flux and the computation of spectra are separate steps.

For the surface flux, one solves the TDSE on the region B and absorbs the solution outside. Absorption can be done at low computational cost and without any distortions. During propagation values and derivatives of $\Psi(\vec{r}_1,\vec{r}_2,t)$ at $|\vec{r}_1| = R_c$ are stored for a sufficiently dense time grid $t_n := n\Delta t$. The storage intervals are determined by the maximal energy $E_{\rm max}$ that one wishes to resolve. The fastest relevant phase oscillations have the period $2\pi\hbar/E_{\rm max}$. One period needs to be sampled at about eight time points, resulting in $\Delta t \approx \pi\hbar/(4E_{\rm max})$. Even for the largest of our applications, file sizes remained within reasonable limits of ~100 GB.

In the second step, using the surfaces stored on file, the integrals (16) are computed for the desired six-dimensional grid of momentum pairs $\vec{k}_1,\vec{k}_2$. The sheer amount of information available in DI spectra makes this an inherently large computation. We use the same grid of $\vec{k}_1^{(\mu)} = \vec{k}_2^{(\mu)}$, $\mu = 1,\ldots,K$ for both momenta. The $\vec{k}_i^{(\mu)}$ can be conveniently chosen on a quadrature grid in polar coordinates, which allows for easy transition to a representation in terms of partial waves.

The scattering amplitudes (18) are accumulated in the following steps:

(a) For given $\vec{k}_1^{(\mu)}$, solve for $\varphi_{\vec{k}_1^{(\mu)}}(\vec{r}_2,t)$, Eq. (21);

(b) at $t = t_n$, get $F(\vec{k}_1^{(\mu)},\vec{k}_2^{(\nu)},t_n)\ \forall\ \vec{k}_2^{(\nu)}$, Eq. (20);

(c) add $F(\cdots)/\Delta t$ into $b(\vec{k}_1^{(\mu)},\vec{k}_2^{(\nu)})$, Eq. (18).

The main computational gain of the method is that the complete, correlated two-electron problem needs to be solved only in the confined domain B. There is no relevant overhead in computing and storing the surface flux.

At long wavelengths and correspondingly low photon energies $\hbar\omega$ the radial extension required for domain B is approximately given by the quiver amplitude $Q := A_{\rm max}/\omega$ of the electron in a field with peak vector potential $A_{\rm max}$ (see Secs. II C and VI B). In contrast, using the standard approach for computing differential DI spectra, the radial extension of the computation box is given by the maximal distance $R_{\rm max}$ that the wave packet can travel until the end of time propagation. This distance is roughly given by the maximal momentum $p_{\rm max}$ times the duration $2\pi n/\omega$ of an n-cycle pulse. For long wavelengths, photoelectron energies extend to 10 times the ponderomotive energy $U_p = A_{\rm max}^2/4$. This corresponds to maximal momentum $p_{\rm max} = \sqrt{2E_{\rm max}} \approx \sqrt{5}A_{\rm max}$. Considering both radial directions, at IR wavelength

the tSurff volume B is reduced by a factor

$$\left(\frac{R_{\max}}{Q}\right)^2 \approx \left(\frac{2\pi n\sqrt{5}A_{\max}/\omega}{A_{\max}/\omega}\right)^2 \approx 200n^2, \quad (24)$$

comparing to any approach where the full wave function $\Psi(\vec{r}_1,\vec{r}_2,T)$ is required. In particular, we remark that B is independent of pulse duration n, allowing for long pulses with only linear increase in computational cost.

This significant gain for the two-electron computation comes at the expense of the additional steps (a)–(c). Their actual cost depends on the desired momentum range and resolution. The main computational effort is to solve the inhomogeneous ionic TDSE for each $\vec{k}_1^{(\mu)}$, step (a). Note that, contrary to the full two-electron problem, the equations for different $\vec{k}_1$ are not coupled and lend themselves to straightforward parallelization. In addition, the effort for one ionic problem scales as $\lambda^4 I$ as compared to the $\lambda^7 I^2$ scaling of the two-electron problem; compare Sec. II A. One has to consider that also the detail of information contained in the momentum spectra grows as $\lambda^3 I$ and the overall scaling of the problem persists, if one endeavors to retrieve the spectra on the full six-dimensional momentum grid. This is mitigated by the possibility of performing the spectral analysis, steps (a)–(c) only on the subsections of the $(\vec{k}_1,\vec{k}_2)$ space that are of interest. In the more challenging calculations at IR wavelength of $\lambda = 780$ nm, correlated time propagation and spectral analysis took about equal times.

4. Single-ionization spectra

For completeness we show how single-ionization spectra are computed. The function $\chi_{\vec{k}_1}(\vec{r}_1,T)\varphi_{\vec{k}_1}(\vec{r}_2,T)$ is the component of $\Psi(\vec{r}_1,\vec{r}_2,T)$ on S with asymptotic momentum $\vec{k}_1$. The spectral amplitude of a given ionic channel corresponding to the state $\phi^{(I)}(\vec{r}_2)$, $||\phi^{(I)}|| = 1$, is

$$b^{(I)}(\vec{k}_1) \approx \langle \phi^{(I)} | \varphi_{\vec{k}_1}(T) \rangle. \quad (25)$$

For the spectral densities, a factor 2 accounts for the symmetric contributions from S and $\overline{S}$,

$$P^{(I)}(\vec{k}_1) = 2|b^{(I)}(\vec{k}_1)|^2. \quad (26)$$

If DI is negligible, the problem can be further simplified by admitting only contributions from the source (22) that will end up in channel I. We introduce the ionic solution

$$i\frac{d}{dt}\phi^{(I)}(\vec{r}_2,t) = H_{\text{ion}}(t)\phi^{(I)}(\vec{r}_2,t), \quad (27)$$

with a *final* condition at $t = T$,

$$\phi^{(I)}(\vec{r}_2,T) = \phi^{(I)}(\vec{r}_2). \quad (28)$$

With this, the channel source is

$$C^{(I)}_{\vec{k}_1}(\vec{r}_2,t) = \phi^{(I)}(\vec{r}_2,t)\langle \phi^{(I)}(t) | C_{\vec{k}_1}(t) \rangle \quad (29)$$

and $\varphi_{\vec{k}_1}(\vec{r}_2,t) \propto \phi^{(I)}(\vec{r}_2,t)$ fulfills the homogeneous part of Eq. (21) by definition. One readily sees that

$$b^{(I)}(\vec{k}_1,t) = \int_{-\infty}^{T} dt \langle \phi^{(I)}(t) | C_{\vec{k}_1}(t) \rangle. \quad (30)$$

With all surface values for all times available on disk, one can perform the integral starting from T and solve (27) backward in time.

The nonionizing condition will be noted, as also in backward propagation the $\phi^{(I)}(\vec{r}_2,t)$ must remain confined in $[0,R_c]$. Violation of the condition appears as reflections or, in the presence of an absorber, by exponential divergence of the solution, rather than exponential damping.

The simplification is significant, as the ionic solution $\phi^{(I)}(\vec{r}_2,t)$ needs to be computed only once for all $\vec{k}_1$. This approach was used in Refs. [41,50] to compute single-ionization spectra from multielectron systems including core polarization and doubly excited states.

C. Control of convergence

Equation (5) becomes exact only in the limit $T \to \infty$ and $R_c \to \infty$. The effects of truncation at finite T and R_c must be examined for any given physical situation. This holds not only for tSurff, but any method that cannot draw on exact scattering information from other sources. In tSurff, the computational cost increases only linearly with T and therefore convergence with respect to T is usually easily achieved. Convergence with the radial extension R_c of domain B represents a much more difficult task. In the result Secs. V and VI we therefore always demonstrate convergence behavior with the tSurff radius R_c, which strongly depends on the observable of interest.

1. Single-electron convergence

The two-particle version of the tSurff method inherits the convergence properties of its single-particle predecessor [37].

First, contributions to the photoelectron spectrum are only taken into account from those parts of the wave function which passed through the tSurff surface at R_c at time T; see Eqs. (12) and (18). In order to capture low energetic contributions correctly, time propagation must continue until some time after the end of the pulse. This limitation applies whenever a finite domain of the wave packet $\Psi(T)$ is excluded from analysis. All approaches listed above, except for [28], are affected by this.

Second, the truncation of the nuclear potential beyond R_c transforms the Coulomb potential into a short-range potential, where the missing long-range behavior modifies electron trajectories. This is particularly important near thresholds with strong modification of the Rydberg states and low-energy scattering. The nuclear potential truncation is the most severe approximation introduced by tSurff in the single-particle case, and this carries over to the two-particle situation. At the moment, the effects can only be controlled by increasing the truncation radius R_c. It may also be possible to introduce corrections to the scattering wave function $\chi_{\vec{k}}(\vec{r},t)$ and thereby dispose of the nuclear potential truncation completely, which is a goal for future work. We are currently investigating the possibility to replace the pure Volkov waves with Eikonal Volkov waves [49].

Third, highly excited bound states can extend well beyond R_c, which conflicts with the assumption that any wave function part beyond R_c belongs to the continuous spectrum. The effect of a persistent finite probability density at R_c are oscillations of the spectral density with respect to energy and T. Increasing

R_c can reduce these artifacts as the bound-state density decays exponentially. However, for highly excited states this decay is slow and moving to large R_c comes at large computational cost. If the bound states are known well enough, they can be projected out once the pulse is over; see [37]. A generally applicable method to suppress these oscillations is to average the spectral amplitudes over a range of propagation times T, which has proven to be simple and efficient, with quick convergence and little extra computational cost. Details are given in Appendix B.

Fourth, a practical lower limit for the size of the simulation box is set by the quiver radius Q of the motion of a free electron in the laser field: As electrons may return from distance Q into regions of strong interactions to cause, for example, recollisions, the dynamics over the whole region must be included. The infinite-range exterior complex scaling (irECS) absorber used for our computations does, in principle, maintain the full dynamics, but it can do so only if discretized with a large number of coefficients; see [51] and Sec. III C. Rather than placing R_c inside the quiver radius with a generous number of discretization points for irECS, one does better to move R_c to near Q with only a few points for irECS. In this way one also benefits from a better approximation of the long-range Coulomb interaction.

2. Two-electron convergence

Specific for two-electron systems is the error introduced by approximating the asymptotics of the exact scattering solution in product form $\chi_{\vec{k}_1,\vec{k}_2} \approx \chi_{\vec{k}_1}\chi_{\vec{k}_2}$. This error decreases with growing R_c. As the essence of tSurff is to keep R_c as small as possible, it is affected most acutely by this. In the direct approach, the product ansatz is made typically only beyond $|\vec{r}| \gtrsim 100$, either explicitly or implicitly as in Ref. [28]. We show that, depending on the observable in question, tSurff radii as small as $R_c \approx 20$ can give sensible results. Some observables are strongly affected by this approximation: Whenever "postcollision" interaction, i.e., repulsion between electrons far from the nucleus, is important, a product description is bound to fail. This is most pronounced for side-by-side double emission, where the two electrons are in close proximity for long times. The relevant distances depend on the details of the process [52]. If these distances lie beyond practical R_c values, tSurff would need to be amended by fully including postcollision electron-electron interaction [44], but such an approach has not been proven yet in practice.

III. NUMERICAL IMPLEMENTATION

A. Basis

The tSurff method requires the numerical solution of the full two-particle TDSE (3) on domain B and several single-particle TDSEs (21) on domain S. In this section we present our choice for the discretization, discuss its merits, and compare it to other popular choices.

We expand the two-electron wave function on B into single-particle spherical harmonics, $Y_l^m(\Omega) \equiv Y_l^m(\theta,\varphi)$,

$$\Psi(\vec{r}_1,\vec{r}_2,t)|_B = \sum_{l_1m_1}\sum_{l_2m_2} Y_{l_1}^{m_1}(\Omega_1)Y_{l_2}^{m_2}(\Omega_2)R_{l_1m_1l_2m_2}(r_1,r_2,t). \tag{31}$$

For linearly polarized pulses, the magnetic quantum number M is conserved and $m_1 = M - m_2$. The sums are truncated when convergence is reached, an example for the truncation of the l_1-l_2 grid at IR wavelengths is given in Sec. VI F. The numerical single-particle functions $\varphi_{\vec{k}_1}(\vec{r}_2)$ needed in region S [Eq. (21)] are also expanded into spherical harmonics:

$$\varphi_{\vec{k}_1}(\vec{r}_2,t) = \sum_{l_2m_2} Y_{l_2}^{m_2}(\Omega_2)R_{l_2m_2}(r_2,t). \tag{32}$$

The radial functions are discretized by a finite-element method. For $R_{l_1m_1l_2m_2}$ the r_1r_2 plane is divided into rectangular patches $[r_1^{(n_1-1)},r_1^{(n_1)}] \times [r_2^{(n_2-1)},r_2^{(n_2)}]$ and we write

$$R_{l_1m_1l_2m_2}(r_1,r_2) = \sum_{n_1,n_2=1}^{N} R^{(n_1,n_2)}_{l_1m_1l_2m_2}(r_1,r_2,t), \tag{33}$$

where

$$R^{(n_1,n_2)}_{l_1m_1l_2m_2}(r_1,r_2,t) = \sum_{p_1,p_2} f_{p_1}^{(n_1)}(r_1)f_{p_2}^{(n_2)}(r_2)c^{(n_1,n_2)}_{p_1l_1m_1p_2l_2m_2}(t) \tag{34}$$

is expanded into products of one-dimensional finite-element basis functions $f_{p_1}^{(n_1)}(r_1)$ and $f_{p_2}^{(n_2)}(r_2)$. The $f_p^{(n)}(r)$ are high-order polynomials that are confined to the interval $[r^{(n-1)},r^{(n)}]$. The last interval is let to extend to $r^{(N)} = \infty$ with an exponential factor $\exp(-\alpha r)$ with $\alpha \lesssim 1$. We usually choose $R_c = r^{(N-1)}$ and absorption acts only on the last interval; see Sec. III C. An analogous expansion into $f_{p_2}^{(n_2)}$ is used for the single-particle radial functions $R_{l_2m_2}$. This type of radial discretization was introduced in Ref. [51]; also see Appendix C.

Denoting the expansion coefficients for $\varphi_{\vec{k}_1}(\vec{r}_2,t)$ as the components d_j of a vector $\vec{d}$ with the single-electron multi-index $j := (n_2,p_2,l_2,m_2)$, the time evolution of $\vec{d}$ is

$$i\frac{d}{dt}\vec{d}(t) = \widehat{S}_2^{-1}[\widehat{H}_{\rm ion}(t)\vec{d}(t) - \vec{C}(t)], \tag{35}$$

where $\widehat{H}_{\rm ion}$ and $\widehat{S}_2$ are the ionic Hamiltonian and overlap matrices with respect to the single-electron indices j. $\vec{C}$ is the vector of overlaps $\langle j|C\rangle$ of the source term $C(\vec{r}_2,t)$, Eq. (22), with the basis functions $|j\rangle$. In region B, the equation of motion for the expansion coefficients c_i with the two-electron multi-index $i := (n_1,p_1,l_1,m_1,n_2,p_2,l_2,m_2)$ is

$$i\frac{d}{dt}\vec{c}(t) = \widehat{S}^{-1}\widehat{H}(t)\vec{c}(t), \tag{36}$$

where $\widehat{H}(t)$ and $\widehat{S}$ denote Hamiltonian and overlap matrices with respect to i. As the Hamiltonian is local, i.e., it contains only multiplication and differential operators, the localization of the radial basis on the n_1n_2 patches produces block structured matrices $\widehat{H}$, $\widehat{S}$, and $\widehat{H}_{\rm ion}$. Note that the overlap matrix is not the unit matrix $\widehat{S}_{ij} \neq \delta_{ij}$, as the radial basis functions $\{f_k^{(n)}\}$ are not orthonormal.

The ansatz function (34) is not guaranteed to be continuous across the element boundaries $r_i^{(n)}$. Constraining $\vec{c}$ to ensure continuity effectively connects the separate matrix blocks. As a result, one has to solve a linear system of the form $\vec{b} = \widehat{S}^{-1}\vec{a}$ at each time step. Considering the very large basis size, this

may appear a daunting task. Closer inspection shows that the inverse has tensor product form:

$$\widehat{S}^{-1} = \widehat{S}_1^{-1} \otimes \widehat{S}_2^{-1}. \tag{37}$$

Further, the overlap matrices $\widehat{S}_1$ and $\widehat{S}_2$ can be reduced to near-diagonal form, with only two nonzero elements off diagonal for every element boundary point $r_1^{(n_1)}$ and $r_2^{(n_2)}$. The exact inverses of such matrices can be computed as a diagonal with a low rank correction such that the floating operations count becomes negligible. Details are given in Appendix C.

B. Time propagation

For the time integration of Eqs. (36) and (35) we use the standard fourth-order Runge-Kutta (RK4) algorithm with adaptive step size control. Step size control is important because at long wavelengths, depending on intensity, the time evolution can be driven by the external field and strongly vary with the strength of the vector potential $|\vec{A}(t)|$. Experiments with exponential integrators such as Arnoldi and Magnus propagators appear to indicate that these play out their advantages mostly over intervals where the time evolution operator is well approximated by a time-constant matrix exponential. For strong near-IR fields, the gain in time step size cannot outweigh the overhead of these more complex methods.

The rather small, but cheap time steps of the RK4 are no major disadvantage for tSurff, because we want to sample the solution at time intervals Δt that are short for physical reasons; see Sec. II B 3. In fact, we found that the time step returned by the RK4 step size control was typically only factors 5–10 smaller than the required sampling intervals for resolving the full energy range.

This said, it may well be that the use of, for example, higher-order implicit methods or methods for time-dependent matrix exponentiation [53,54] would improve performance.

C. Absorption and choice of gauge

For solving the two-particle TDSE (36) and the single-particle TDSEs (35) we want to start absorption right at R_c to minimize the computational effort. For correct results, the absorber must be perfect, as any reflections immediately corrupt the surface values. We employ irECS [51] for this purpose. Exterior complex scaling (ECS) is an analytical continuation method and has the useful property to preserve (in principle) the full information of the dynamics even in the absorbing region. This allows for particle reentry from the scaled into the unscaled region, although in numerical computations excessive excursion into the scaled region will lead to accumulation of numerical errors. Typically, small tails of rescattering wave packets moderately extending into the absorbing region are sufficiently undisturbed, which allows for box sizes R_c close to or even below the quiver amplitude Q. Numerical evidence for this fact was given in Ref. [51]. irECS is a particular form of discretizing ECS that gives perfect absorption with about 20 discretization coefficients on each radial coordinate.

Note that ECS only works with suitable interactions. It can be used in the velocity gauge representation of the dipole operator $i\vec{A}(t)\cdot\vec{\nabla}$, but not in length gauge $\vec{E}(t)\cdot\vec{r}$. Fortunately, velocity gauge is also numerically favored for strong field problems [42,55].

Implementation of irECS in a finite-element scheme is straightforward [51]; details can be found in Appendix E. In time-independent situations, standard ECS has been applied also with other discretizations, including FE-DVR [46]. Severe problems of accuracy and stability had been reported for ECS when applied to the TDSE using FE-DVR discretizations [56]. Only recently we observed that the reported errors are not related to ECS and that standard ECS as well as irECS can be applied in finite difference and FE-DVR schemes with comparable efficiency as in the present finite-element implementation [57].

D. Electron-electron interaction

When solving the TDSE (36) on domain B, the electron-electron interaction represents the major computational challenge. It is the only part of the Hamilton operator that does not factorize into tensor products with respect to the two particles. Using the multipole expansion we can express the matrix connecting the radial (n_1,n_2) patch with (n_1',n_2') as

$$\begin{aligned}
&\left\langle \Psi^{(n_1'n_2')}_{l_1'm_1'l_2'm_2'} \middle| \frac{1}{|\vec{r}_1-\vec{r}_2|} \middle| \Psi^{(n_1n_2)}_{l_1m_1l_2m_2} \right\rangle \\
&\quad = \sum_{\lambda\mu} \frac{4\pi}{2\lambda+1} \left\langle Y^{m_1'}_{l_1'} Y^{\mu}_{\lambda} \middle| Y^{m_1}_{l_1} \right\rangle \left\langle Y^{m_2'}_{l_2'} \middle| Y^{\mu}_{\lambda} Y^{m_2}_{l_2} \right\rangle \\
&\qquad \times \underbrace{\left\langle R^{(n_1'n_2')}_{l_1'm_1'l_2'm_2'} \middle| \frac{\min(r_1,r_2)^{\lambda}}{\max(r_1,r_2)^{\lambda+1}} \middle| R^{(n_1n_2)}_{l_1m_1l_2m_2} \right\rangle}_{=:\widehat{V}^{(\lambda)}}.
\end{aligned} \tag{38}$$

The electron-electron interaction matrix is full except where symmetry forbids transition and cannot be strictly decomposed into a short sum of tensor products. For finite angular expansion, the sum over λ,μ remains finite and, in many cases, can be truncated at relatively low λ without introducing relevant numerical error. The operations count for matrix-vector application scales $\propto P^4$ for a radial expansion of maximal degree $P-1$. This is larger than for all other terms in the Hamiltonian, which have tensor product structure with operations count $\propto P^3$.

However, as pointed out in Ref. [46], in a polynomial basis the scaling can be reduced to P^3. In Appendix D it is shown that the radial multipole matrices $\widehat{V}^{(\lambda)}$, Eq. (38), can be exactly represented by a multiplication on an R-point quadrature grid $(R := 2P-1)$ that is independent of λ,

$$\widehat{V}^{(\lambda)} = (\widehat{T}^{(n_1)} \otimes \widehat{T}^{(n_2)})^{\mathsf{T}} \widehat{D}^{(\lambda)} (\widehat{T}^{(n_1)} \otimes \widehat{T}^{(n_2)}), \tag{39}$$

where he transformation matrices $\widehat{T}^{(n_i)}$ are $R \times P$ and $\widehat{D}^{(\lambda)}$ is a *diagonal* $R^2 \times R^2$ matrix. Applying (39) to a radial coefficient vector of length P^2 has the operations count $2PR(R+P) + R^2$. In practice, one can admit a minor quadrature error and reduce the quadrature grid to $R = P$ points without compromising any of the results reported below. Be cautioned that $\widehat{D}^{(\lambda)}$ is not just $\min(r_1,r_2)^{\lambda}/\max(r_1,r_2)^{\lambda+1}$ evaluated on the quadrature grid points. Its correct form together with other details of the procedure are given in Appendix D.

E. Computational resources

At XUV wavelength tSurff computations can be performed on the workstation scale. For example, on a 16-core shared-memory machine the computation of the two-photon DI cross section (see Sec. V A) took about 12 h with $R_c = 30$a.u. and about 60 h with $R_c = 80$a.u. for each photon energy.

Resource requirements are not significantly increased by the addition of a weak IR field as in Sec. VI A: With a total of 551 partial waves on a 16-core machine, the largest computation with $R_c = 25$ ran for a maximum of 2 days.

Computations at strong IR fields are the most challenging. Yet, the largest of the computations reported in Sec. VI B used 128 cores, running for 10 days in an MPI parallelized scheme for solving the full two-electron problem on domain B; see Sec. II B 3. An additional 5 days were required to compute the solutions on domain S for a $\vec{k}_1$-$\vec{k}_2$ grid dense enough for extraction of the fully differential data.

This should be put into relation to the much larger computing facilities employed in the direct approaches. For example, Ref. [36] used 4000 cores for computations including only 295 partial waves at a weak IR field (no run times are quoted). Resource consumption was not reported in Refs. [9,28,34,48,52], but in all cases computations were performed at supercomputing centers using large-scale machines.

F. Other implementation options

Several other strategies for the discretization and time propagation of the TDSE have been applied in the literature. In Refs. [9,36,48] the TDCC scheme [45] and FE-DVR [46,47] were used. In Refs. [33–35] finite differences were used for discretization; in Ref. [29] B splines were used.

For time propagation, more sophisticated procedures were chosen than the present RK4: the short iterative Lanczos method [58] in Ref. [9], the real-space-product algorithm [59] in Ref. [36], or a Crank-Nicolson method in Ref. [46]. For the time propagation we keep the simple choice for the reasons discussed above.

We chose full finite elements as a discretization for the present calculations, because tSurff had been proven to function in this framework. The compatibility of the tSurff method with other discretizations has been investigated only recently [57]. In view of these recent results, FE-DVR appears to bear the potential for further dramatic reduction of operations count and improve the scalability of tSurff on parallel machines.

There are several other optimizations one can think of, like low-rank description of the electron-electron interaction at large distances, a nonsquare spatial domain for B, or alternative time propagators. Investigation of these technical options is, however, not the purpose of this paper.

IV. OBSERVABLES

Here we introduce the various physical quantities which will be examined in the following result sections. All observables are derived from the fully, fivefold differential photoelectron spectrum, which we refer to as the two-electron probability density,

$$P(E_1,E_2,\Omega_1,\Omega_2) = k_1 k_2 P(\vec{k}_1,\vec{k}_2). \tag{40}$$

For the linearly polarized pulses considered here, the spectra are independent of the sum of the azimuthal angles $\varphi_1 + \varphi_2$. The $E_i = k_i^2/2$ are the final kinetic energies and $\Omega_i := (\theta_i,\varphi_i)$ are the emission angles. The total DI yield is given by

$$Y := \iiiint dE_1 dE_2 d\Omega_1 d\Omega_2 P(E_1,E_2,\Omega_1,\Omega_2). \tag{41}$$

In the regime of multiphoton perturbation theory, one can define the total N-photon cross section as

$$\sigma_N := \frac{\omega^N Y}{\int dt\, I(t)^N}, \tag{42}$$

where $I(t)$ is the laser intensity profile and ω is the photon energy (see [9,30] and references therein). Another popular quantity is the triply differential cross section (TDCS) defined as

$$\frac{d\sigma_N}{dE_1 d\Omega_1 d\Omega_2} := \frac{\omega^N}{\int dt\, I(t)^N} \int dE_2 P(E_1,E_2,\Omega_1,\Omega_2), \tag{43}$$

which is usually evaluated for coplanar geometry, $\varphi_1 - \varphi_2 = 0$ or $=\pi$.

This observable is experimentally accessible as a nuclear recoil momentum distribution, as summarized in Ref. [30]. These cross sections take into account the Fourier width of the pulse by the energy integrations. Therefore, as long as the photon energy is defined sharply enough that no alternate reaction channels open up, they are in good approximation independent of the exact pulse shape.

In contrast, the energy probability distribution, given by

$$P(E_1,E_2) := \iint d\Omega_1 d\Omega_2 P(E_1,E_2,\Omega_1,\Omega_2), \tag{44}$$

sensitively depends on the exact pulse shape, as was noted in Ref. [9], and is shown below. The same holds true for the coplanar joint angular distribution (JAD) at fixed energies E_1 and E_2,

$$P_{E_1,E_2}(\theta_1,\theta_2) := P(E_1,E_2,\Omega_1,\Omega_2)|_{\varphi_1=\varphi_2}. \tag{45}$$

Here it is convenient to consider $P_{E_1,E_2}(\theta_1,\theta_2)$ on $[0,2\pi] \times [0,2\pi]$, where $\theta_1 = \theta_2$ is emission into the same direction, "side-by-side," and $\theta_1 = \theta_2 + \pi$ is emission into opposite directions, "back-to-back." Note, that JADs as defined in [30,32] included an energy integral, as is appropriate for studying one- or two-photon DI. In the nonperturbative regime, where neither N-photon cross sections nor TDCSs are meaningful, direct evaluation of the differential probability density $P(E_1,E_2,\Omega_1,\Omega_2)$ is more adequate.

A. Quantifying spectral correlation

We introduce a measure for angular correlation by a principal component analysis. Sampling the JAD at fixed energies E_1, E_2 on angular grids $\theta_1^{(\mu)}$ and $\theta_2^{(\nu)}$, $\mu,\nu = 1,\ldots,\mathcal{A}$ we obtain an $\mathcal{A} \times \mathcal{A}$ matrix,

$$\widehat{P}_{\mu,\nu} = P_{E_1,E_2}\left(\theta_1^{(\mu)},\theta_2^{(\nu)}\right). \tag{46}$$

A singular value decomposition reveals to what extent $\widehat{P}$ can be factorized into a product of two (or a few) independent

single-particle distributions on the $\theta_1^{(\mu)}$ and $\theta_2^{(\nu)}$ coordinates:

$$\widehat{P}_{\mu,\nu} = \sum_{\alpha=1}^{\mathcal{A}} s_\alpha p_\mu^\alpha q_\nu^\alpha. \tag{47}$$

If only a single term contributes to the sum, there is no correlation between the two angles, and the more terms are needed, the more correlation we will assign to the emission pattern. We normalize single-particle distributions as $\sum_\mu (p_\mu^\alpha)^2 = \sum_\nu (q_\nu^\alpha)^2 = 1$, and define a measure for the "length" of the sum over α as (compare, e.g., [60])

$$C := \frac{(\sum_\alpha s_\alpha)^2}{\sum_\alpha s_\alpha^2}. \tag{48}$$

For a single nonzero s_α there is no correlation and $C = 1$; for constant s_α, C is maximal. For sufficiently dense sampling, C is independent of $\mathcal{A}$.

We would like to point out that this measure of correlation is readily applicable to experimental data. In this way the discussion of whether processes occur with strong or little correlation can be put to a direct experimental test, independent of the analysis presented in this paper.

V. DOUBLE IONIZATION AT XUV WAVELENGTHS

We first present results at short wavelengths. At low computational effort we reproduce a large body of results available in literature and confirm simple theoretical expectations.

Our method requires the numerical solution of Eqs. (36) and (35), whose convergence depends most notably on the number of partial waves included [Eq. (31)] and on the total number of radial coefficients in the finite-element scheme [Eq. (34)]. For short wavelengths, the demand on those discretization parameters is moderate and a multitude of publications with numerical solutions of the TDSE exist. All our results presented in this section are converged to 1% or better with respect to angular and radial expansion. The variational upper bound for the helium ground-state energy is always below −2.902a.u., which compares well to the exact ground-state energy of $E_0 = -2.9037$a.u.

Propagation times are $T \geqslant 8$ fs after the end of the pulse, which gives ample time to remove artifacts of Rydberg states by averaging over T; see Sec. II C. The dominant convergence parameter for this section is the tSurff radius R_c, for which we demonstrate convergence of the short wavelength computations explicitly. As described in Sec. II B, in the present implementation of tSurff the Coulomb potentials are truncated at R_c [Eq. (15)]. In the present section truncation is over an interval of fixed length 4a.u. with smoothing function $f_{[R_c-4,R_c]}$.

Unless indicated otherwise, results in this section were computed with the pulse shape used in Ref. [9], which allows for direct comparison,

$$A(t) \propto \cos^2\left(\frac{\omega t}{2n}\right)\sin(\omega t), \tag{49}$$

for times $-n\tau/2 \leqslant t \leqslant n\tau/2$, where $\omega = 2\pi/\tau$ is the carrier frequency and $n\tau$ is the total duration of the pulse. The $\cos^2$ envelope is, however, not ideal for emulating realistic experimental pulses as the spectral decomposition contains spurious side bands; see, for example, [29]. These produce artifacts in single-ionization spectra and also in DI energy probability distributions. We demonstrate below that with a pulse envelope that better resembles a Gaussian, such as $\cos^8$, the artifacts disappear.

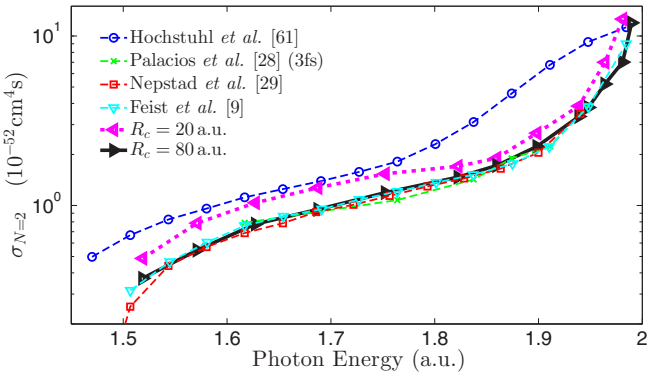

FIG. 2. Total two-photon DI cross section as a function of the photon energy. Results with $R_c = 80$a.u. and pulse duration 4 fs and peak intensity $I = 10^{12}$ W/cm^2 (solid line) agree with Refs. [9,28,29] (dashed lines). Already with $R_c = 20$a.u. (dotted line) good qualitative agreement is reached.

A. Two-photon double-ionization cross section

Exposing a helium atom to a laser field with photon energies $\hbar\omega$ larger than half the DI threshold (1.45a.u.) leads to two-photon DI. At photon energies below the second ionization threshold $\hbar\omega < 2$a.u. DI necessarily involves electron correlations. In this regime full agreement among the numerous theoretical approaches [8,9,22,25,28,29,61–67] has not yet been achieved, not even for the fully integrated total two-photon DI cross section $\sigma_{N=2}$, Eq. (42).

Figure 2 shows a selection of recent results where approximate agreement emerges. In Ref. [61] the time-dependent full configuration interaction method was applied using pulses with a bandwidth of ≈0.15a.u.. The authors attribute the large deviation from most other calculations to their method of extracting DI spectra, as well as to the large spectral width of their pulse. Far from threshold there is good agreement among Refs. [9,28,29,66,67] and with our calculations for $R_c \geqslant 30$, but already at $R_c = 20$ we obtain qualitatively correct results.

The divergence of the results [9,22,28,61] is largest near the threshold $\hbar\omega \lesssim 2$a.u., where the numerical distinction between low-energy sequential processes and correlated double emission becomes blurred. Clearly, in this regime results also depend on the spectral width of the pulse. At $R_c = 80$ we estimate our convergence error to be $\lesssim$5% and find agreement with Refs. [9,28,29]. Note that the longest pulse duration of Ref. [28] is 3 fs rather than the 4 fs of Ref. [9]. We verified that the larger spectral width changes the ratio by less than 3% for the data point $\hbar\omega = 53$ eV $= 1.95$a.u., which is the value closest to threshold in Ref. [28]. The data closest to threshold are found in Ref. [9], where we also agree.

B. Energy probability distribution

Inspecting the angle-integrated energy probability distributions $P(E_1, E_2)$ one sees pronounced two-electron

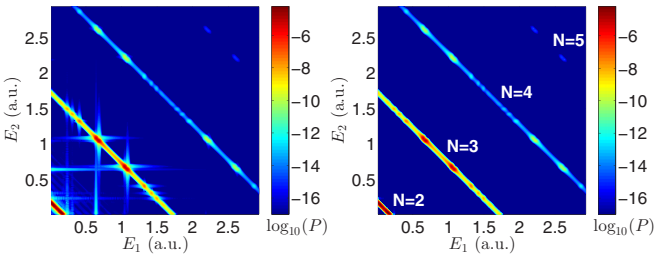

FIG. 3. (Left) Energy probability distribution $P(E_1,E_2)$ for a $n = 120$ cycle pulse with photon energy $\hbar\omega = 42$ eV and peak intensity $I = 10^{13}$ W/cm^2 for a cos^2 pulse envelope. (Right) Calculation with a cos^8 envelope of the same FWHM. Structures generated by the cos^2 sidebands disappear.

multiphoton lines (cf. Fig. 3) where the electrons share the total energy $E_1 + E_2 = E_0 + N \cdot \hbar\omega$, $N = 2,3,\ldots$, of N absorbed photons. The two-photon cross section σ_2 is the integral over the $N = 2$ shared energy line. Along the $N \geqslant 3$ shared energy lines local maxima are found, which is a signature of sequential, uncorrelated double emission. This is the case if one electron overcomes the first ionization potential $I_p^{(1)} \approx 0.9$a.u. ending up with energy $E_1 = -I_p^{(1)} + n\hbar\omega$, $n = 1,2,\ldots$, and in an separate step the second electron gets detached from the ion by the absorption of two or more photons with final energy $E_2 = -I_p^{(2)} + m\hbar\omega$, $m = 2,3,\ldots$. This process was dubbed "double ionization above threshold ionization" (DI-ATI) [68]. Other local maxima along the shared energy lines involve intermediate excited ionic states; see Sec. V D.

All these features can be seen in the energy probability distribution, shown in Fig. 3 for the photon energies $\hbar\omega = 42$ eV ~ 1.54a.u.: The $N = 2$ shared energy line at $E_1 + E_2 \approx 0.2$a.u. does not have particular structure, while the $N = 3$ line at $E_1 + E_2 \approx 1.7$a.u. shows pronounced sequential peaks at $(E_1,E_2) \approx (0.6,1.1)$a.u. and $\approx(1.1,0.6)$a.u. and similar at $N = 4$.

Figure 3 also demonstrates the effect of the pulse envelope by replacing the cos^2 envelope (49) with a cos^8 one with the same full width at half maximum. The cos^2 envelope produces extra DI structures that can hardly be considered as physical. Such artifacts were already observed in Ref. [68], but their origin was not linked to envelope effects. Both computations in Fig. 3 used $R_c = 20$a.u. and $T = 1$ ps. By the long time propagation any artifacts from Rydberg states are safely suppressed (Sec. II C and Appendix B).

C. Angular distributions

The TDCS, Eq. (43), was calculated for $N = 2$ at $E_1 = 0.092$a.u. $= 2.5$ eV where contributions of equal energy sharing $E_1 \approx E_2$ dominate. The TDCS, as most angle- and energy-resolved quantities, is rather sensitive to R_c as it is strongly affected by postcollision interactions [52]. In Fig. 4 it can be seen that, for equal energy sharing, even with a box size of $R_c = 80$a.u., there remain minor quantitative discrepancies with Ref. [9]. The zero in the cross section for side-by-side emission ($\theta_1 = \theta_2$) is reproduced if electron-electron repulsion can act also far from the nucleus. One can directly see that electron repulsion rather than total box size is responsible, by

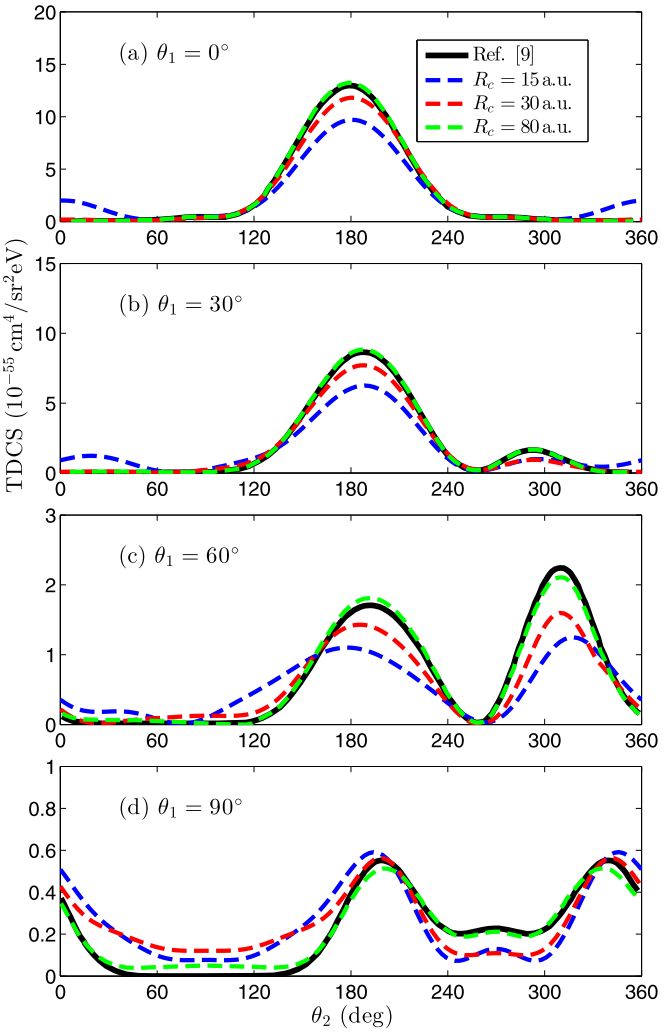

FIG. 4. Triply differential cross section for two-photon DI of He at photon energy $\hbar\omega = 42$ eV and equal energy sharing for different tSurff radii R_c. The same pulse parameters as in Ref. [9] were used.

performing computations with $R_c = 80$a.u. but suppressing electron-electron for all $r_1,r_2 > 30$a.u., which reproduces the $R_c = 30$a.u. results.

The coplanar JADs (45) provide a two-dimensional differential view on the cross sections (43), which reveals a pronounced energy dependence of the emission patterns. In Fig. 5 two exemplary JADs are shown. At the equal energy sharing point $(E_1,E_2) \approx (0.86,0.86)$a.u. for three absorbed photons, we observe side-by-side $\theta_1 \approx \theta_2$ emission; see Fig. 5(a). Back-to-back emission is suppressed due to selection rule C stated in Ref. [69]: Because the three-photon photoelectron states are odd, they have a node at $\vec{k}_1 = -\vec{k}_2$.

To contrast this, we picked as a second point the sequentially accessible energies $(E_1,E_2) \approx (1.09,0.64)$a.u. [Fig. 5(b)], where emission is almost completely uncorrelated (see also next section) and well described by the simple angular distribution $P(\theta_1,\theta_2) \sim |Y_2^0(\theta_1)Y_1^0(\theta_2)|^2$. Qualitatively, these structures are already reproduced with box sizes as small as $R_c = 15$a.u.

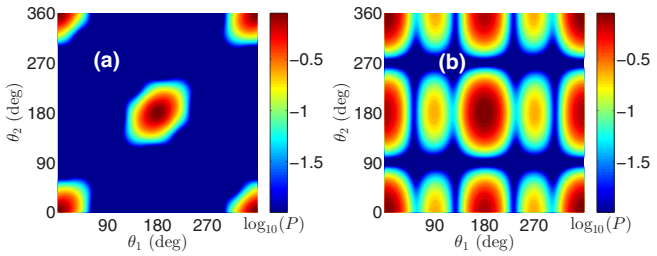

FIG. 5. (Left) Correlated side-by-side emission at three-photon equal energy sharing. (Right) Uncorrelated three-photon sequential ionization at $(E_1,E_2) \approx (1.09,0.64)$a.u. Plots are normalized to $\max_{E_1,E_2}[P(E_1,E_2)] = 1$.

D. Angular correlation

We already classified, by visual inspection, the angular distributions shown in Fig. 5 as correlated or uncorrelated. For a more quantitative description we use the correlation measure defined in Eq. (48).

In Fig. 6(a) we show the probability distribution evaluated along the $N = 3$-photon shared energy line of Fig. 3. The JADs in Fig. 5 correspond to the points $\Delta E := E_1 - E_2 = 0$ and $\Delta E \approx 0.45$a.u. Apart from the purely sequential peaks at $(E_1,E_2) = (-I_p^{(1)} + \hbar\omega, -I_p^{(2)} + 2\hbar\omega)$, there are several more peaks corresponding to excited states of the He^+ ion. Denoting by $\mathcal{E}_n$ the excitation energy from the ionic ground state to the nth excited state, the DI efficiency is enhanced at energies $(E_1,E_2) = (-I_p^{(1)} + 2\hbar\omega - \mathcal{E}_n, -I_p^{(2)} + \hbar\omega + \mathcal{E}_n)$

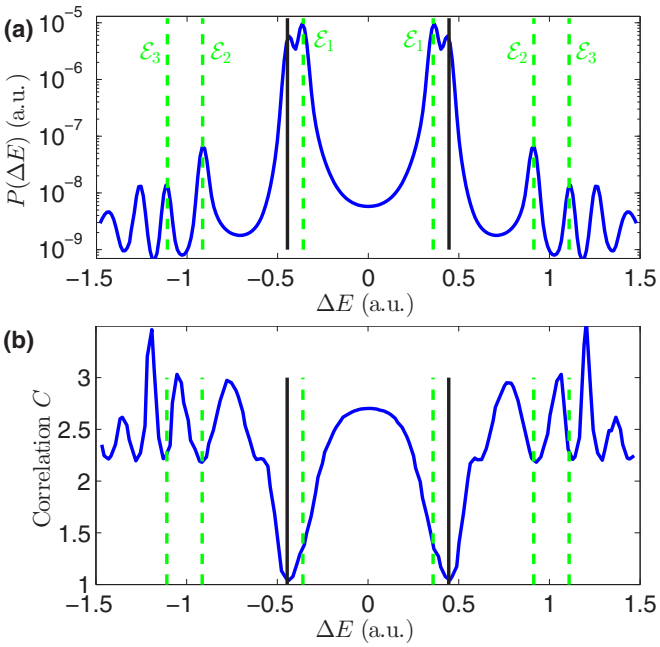

FIG. 6. (Top) Probability distribution $P(E_1,E_2)$ shown in Fig. 3 along the $N = 3$-photon line as a function of the energy difference $\Delta E := E_1 - E_2$. (Bottom) Angular correlation C [Eq. (48)] along the same line. Vertical lines: sequential peaks involving the ionic ground state (solid) and excited ionic states (dashed). The minima for higher ionic excitations are slightly displaced due to the cutoff of the Coulomb potential at $R_c = 20$a.u.

with $n \in \mathbb{N}$; also see [48]. As the photon energy $\hbar\omega \approx 1.54$a.u. is nearly resonant with the first excitation energy $\mathcal{E}_1 = 1.5$a.u., the resonant and the purely sequential peaks are barely discernible.

The degree of correlation along the three-photon shared energy line features a minimum for each maximum of the DI probability. As expected, correlation is reduced when the transition goes through an intermediate state that disentangles the detachment of the two electrons. In particular, the value for no correlation $C = 1$ is almost reached at the sequential point $\Delta E = 0.45$, where the angular distribution is well described as $\propto |Y_2^0 Y_1^0|^2$ [Fig. 5(b)].

VI. DOUBLE IONIZATION AT INFRARED WAVELENGTHS

A. Two-color XUV-IR double emission

Published results of *ab initio* computations for DI photoelectron *spectra* at IR wavelengths treat situations where an XUV pulse initiates dynamics and a weak IR pulse controls the ionization of the excited system. For example, in Ref. [32] an IR pulse with intensity 3×10^{12} W/cm^2 was used to modify the angular distributions of single- and two-photon DI by an XUV pulse. In Ref. [33] time-dependent ionization yields at large intensities were computed, but the used method did not allow for computation of DI spectra.

In Ref. [36] an attosecond XUV pulse with photon energy $\hbar\omega = 1.5$a.u. tuned to the lowest He^+ transition energy was used to enhance photo absorption from a single-cycle IR dressing pulse of moderate intensity 2×10^{14} W/cm^2. It was found that at time delays between the IR field and the XUV pulse coinciding with recollision events excessive absorption of IR photons is induced by the strong electron-electron correlation.

Figure 7 shows our results for the probability density at total emission energy $E_{\rm tot} = E_1 + E_2$,

$$P(E_{\rm tot}) = \int_0^{E_{\rm tot}} dE_1 P(E_1, E_{\rm tot} - E_1). \qquad (50)$$

The top panel shows the enhancement across the whole energy range. The bottom panel singles out $E_{\rm tot} = 60$ eV as a function of delay time. We reproduce the overall picture reported in Ref. [36], but find significant quantitative discrepancies. Note that the comparison is not in absolute numbers, as results of [36] are given in arbitrary units. For example, at larger positive offsets Ref. [36] shows nearly constant data points for large positive offsets, which does not match with our computations. Such a behavior may appear implausible, as at these delays the IR has nearly passed when the XUV arrives, and yields should fall to the very low level of pure XUV DI at $E_1 + E_2 = 60$ eV. We would like to remark that the simulation box size of 305a.u. used in Ref. [36] falls short of the distance of $\gtrsim$400a.u. that 60-eV electrons travel during the IR pulse duration. For tSurff, the cutoffs at $R_c \leqslant 25$a.u. used in our simulations would mask long-range Coulomb and postcollision effects; however, the impact of R_c appears to be small; see Fig. 7.

B. Double-ionization enhancement by recollision

To this date, DI at IR wavelength has not been reproduced by solutions of the two-electron TDSE for the the full intensity

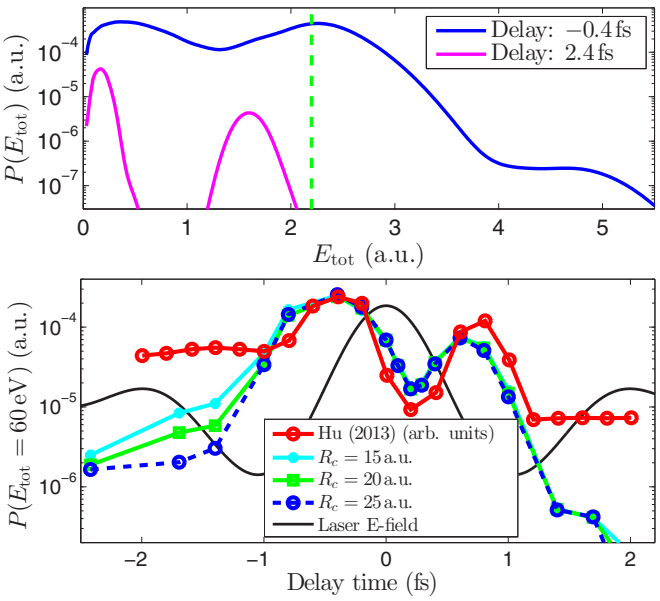

FIG. 7. (Top) Photoelectron spectrum as a function of the shared total energy [Eq. (50)] for two relative time delays between XUV and IR pulses. Large positive time delays correspond to the XUV pulse coming after the IR pulse. The green dashed line indicates $E_{\rm tot} = 60$ eV. (Bottom) $P(E_{\rm tot} = 60\,{\rm eV})$ as a function of the relative time delay: dependence on R_c and comparison with Ref. [36]. Arbitrary units in Ref. [36] are adjusted to approximately match our results.

range because of the high demand on computational resources; see Sec. II A. Using tSurff, we can provide yields up to intensities 4×10^{14} W/cm^2, with error estimates of $\lesssim$20% up 3.5×10^{14} W/cm^2, using only moderate computational resources.

1. Double- to single-ionization ratio

The ratio of double- to single-ionization yields is shown in Fig. 8 for R_c up to 30a.u. and compared to experiment. Except

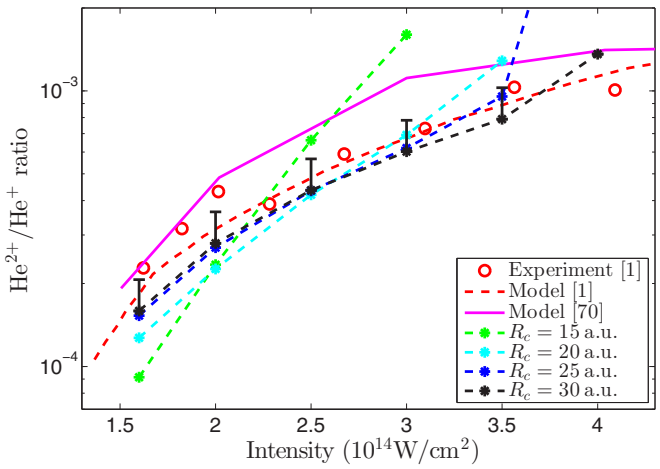

FIG. 8. Ratio of DI yield and single-ionization yield as a function of intensity. Experiment and model [1], model calculations [70], and our full two-electron results for increasing R_c. Upward error bars indicate the long pulse limit.

for R_c, our results are converged with respect to all other discretization parameters to within a few percent. We used a laser pulse with single-cycle rampup, n cycles at full intensity, and one cycle rampdown at wavelength $\lambda = c\tau = 780$ nm,

$$A(t) \propto f_{\alpha,\beta}(-t)\sin(2\pi t/\tau) f_{\alpha,\beta}(t), \tag{51}$$

with $\alpha = n\tau/2$, $\beta = (n/2+1)\tau$ and $f_{\alpha,\beta}$ as in Eq. (15). The calculations were performed with pulse durations of $n = 4$ cycles.

Figure 8 shows the double-to-single ratio as obtained with $R_c = 15$, 20, 25, and 30a.u. and smoothing $R_c - \alpha = 3$, 4, 6, and 8a.u., respectively; see Eq. (15). One can clearly see that larger intensities require larger R_c, which roughly correlates with the quiver radius Q. In the intensity range 1.6–3 $\times 10^{14}$ W/cm^2 with quiver radii $Q = 20$–27a.u. results vary by at most 25% between $R_c = 20$a.u. and $R_c = 30$a.u. At the intensities $I \geqslant 3.5 \times 10^{14}$ W/cm^2, numerical results for $R_c < 30$a.u. strongly depart from our largest calculation with $R_c = 30$a.u. The lower intensity limit for our calculations is $\lesssim 1.5 \times 10^{14}$ W/cm^2, where the overall yields are so small that numerical inaccuracies render the results useless.

There is some dependence of our results on the pulse duration: Using a two-cycle rampup we found changes of less than 5% at selected intensities. More important is the dependence on pulse duration. At the intensities $\leqslant 2.5 \times 10^{14}$ W/cm^2 we found an increase of ratio for $n = 4,5,\ldots$ cycles, which saturates at about 30% for $n \approx 8$ with no relevant further increase for durations up to $n = 12$. We expect similar pulse duration dependence at higher intensities. This increase by 30% is indicated by an (upward) error bar for our $R_c = 30$a.u. calculation in Fig. 8.

Figure 8 also shows the experimental results and model predictions. There is good agreement with the experimental data, but that may well be fortuitous, as experimental intensities were subjected to errors as large as 30%. The analytical model of Ref. [1] is based on the single active electron approximation (SAE) and on the ac-tunneling (ADK) rates [71] and is, by its construction, close to the experimental data. The model in Ref. [70] implements the rescattering scenario using the SAE approximation in combination with electron-ion impact cross sections. It appears to somewhat overestimate the actual ratio, as it remains outside our estimated tSurff error. Note that in the plot shown in Fig. 1 of Ref. [70], experimental intensities are scaled by a factor 1.15 for the purpose of the comparison.

2. Energy probability distributions

In Fig. 9 we present energy probability distributions $P(E_1,E_2)$ for IR DI at intensities $I = 1.6,2.5,3.5$ and 4×10^{14} W/cm^2, with the pulse shape as in Fig. 8 for photoelectron energies $E_1, E_2 < 3U_p$. One sees that the four-cycle pulses define the carrier frequency ω well enough to clearly distinguish individual DI-ATI peaks separated by the photon energy $\hbar\omega$. One also observes changes in the DI emission pattern with increasing intensity I. In Figs. 9(a) and 9(b) conspicuous enhancement of double emission in the area $E_1 \approx E_2 \approx 1.7U_p$ appears. Note that at the corresponding intensities 1.6 and 2.5×10^{14} W/cm^2 the maximal recollision energy remains below the second ionization potential of 2a.u. As recollision cannot be the sole DI mechanism, one may speculate that

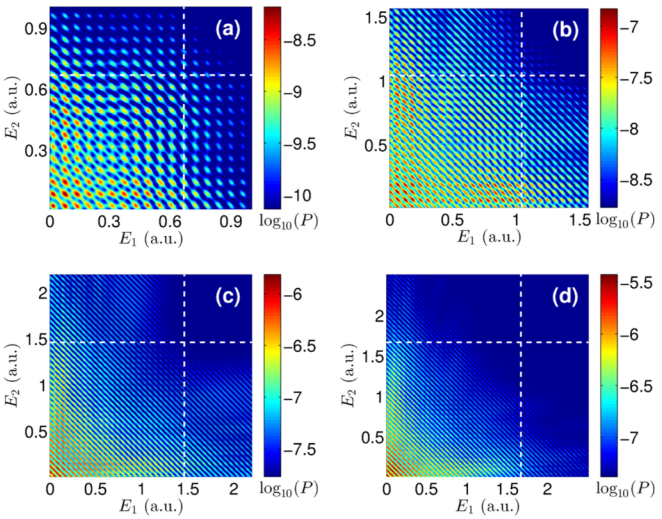

FIG. 9. Total DI spectra $P(E_1, E_2)$ [Eq. (44)] for several of the data points with truncation interval $R_c = 30$a.u. shown in Fig. 8. Intensities in units of 10^{14} W/cm^2 are (a) 1.6, (b) 2.5, (c) 3.5, and (d) 4.0. White dashed lines mark $2U_p$.

processes like simultaneous tunneling and doubly delayed emission (DDE) [7], where final energies E_1 and E_2 are comparable, play a greater relative role. At (c) and (d) direct excitation by the recolliding electron becomes accessible and a roughly L-shape energy distribution emerges.

For estimating the R_c-induced errors of the energy distributions we define the relative difference $\mathcal{E}$ between two distribution P_a and P_b as

$$\mathcal{E}(E_1, E_2) := \frac{|P_a(E_1, E_2) - P_b(E_1, E_2)|}{\overline{P}_{\hbar\omega}(E_1, E_2)}, \qquad (52)$$

where $\overline{P}_{\hbar\omega}(E_1, E_2) := \max_{E_1', E_2'} P(E_1', E_2')$ denotes the maximum over a $\hbar\omega$ neighborhood with $(E_1' - E_1)^2 + (E_2' - E_2)^2 < (\hbar\omega)^2$.

Two examples are shown in Fig. 10. At $I = 2 \times 10^{14}$ W/cm^2 with quiver radius $Q = 22$ a.u. we compare calculations with $R_c = 25$ a.u. and $R_c = 35$a.u. [Fig. 10(a)]. Relative differences approach 60%, where one electron has low energy and also near the energy diagonal. These regions can be expected to be strongly affected by Coulomb truncation. In many areas differences remain below 20%. The intensity $I = 3.5 \times 10^{14}$ W/cm^2 is near the limit of our presently

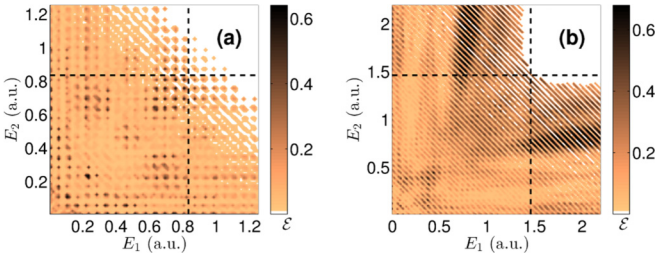

FIG. 10. Error estimates $\mathcal{E}$ by comparing computations with (a) radii $R_c = 25$a.u. vs $R_c = 35$a.u. for $I = 2 \times 10^{14}$ W/cm^2 and (b) $R_c = 25$a.u. vs $R_c = 30$a.u. for $I = 3.5 \times 10^{14}$ W/cm^2. Errors are only plotted where $P(E_1, E_2)$ is larger than 1% of its maximum.

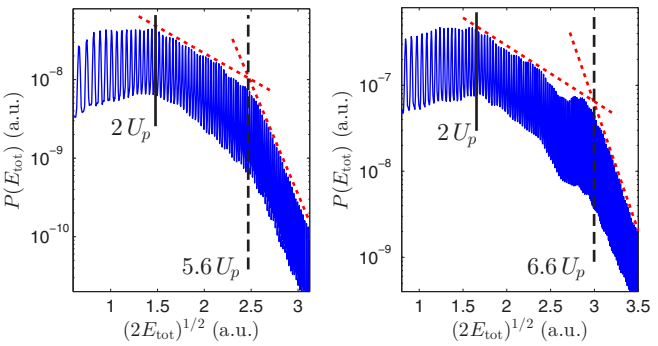

FIG. 11. Total momentum spectrum $P(E_{\rm tot})$ [Eq. (50)] for a 780 nm $n = 4$ cycle pulse. (Left) 2.6×10^{14} W/cm^2 cutoff at $5.6U_p$. (Right) 3.25×10^{14} W/cm^2 cutoff at $6.6U_p$. Solid lines mark the momentum corresponding to $2U_p$; dashed lines mark the transition to the exponential decay at the cutoff of the spectrum; dotted lines indicate the slopes. The behavior conforms with Fig. 3 of [34] for 390 nm at the corresponding intensities 1.04×10^{15} W/cm^2 and 1.3×10^{15} W/cm^2.

accessible parameter range [Fig. 10(b)]. At this intensity the quiver radius $Q = 29$ a.u. exceeds the truncation radius $R_c = 25$. Still, comparing to $R_c = 30$ a.u., relative differences approach 60% only at few places in the relevant region $E_1 + E_2 \leqslant 2U_p$ and are mostly below 30%. Large relative differences naturally appear where yields become small.

In Ref. [34], a sharp transition of the cutoff in the shared DI energy distribution from $5.3U_p$ to $> 7U_p$ was found, when maximum recollision energies surpass $I_p^{(2)} = 2$ a.u. at $\lambda = 390$ nm. A similar cutoff was reported in Ref. [72] for a one-dimensional model. We could reproduce this for 390 nm (not shown) and find the cutoff also in full three dimensions at 780 nm; see Fig. 11.

C. Angular distribution

JADs depend most sensitively on R_c and full convergence could not be achieved with moderate computational effort. In Fig. 12 we show JADs for three different (E_1, E_2) at $I = 2 \times 10^{14}$ W/cm^2. In panel (b) it can be seen that if both electrons escape with large energies the angular emission pattern is uncorrelated and highly focused around the polarization axis. If one electron barely manages to escape, then its angular distribution is less focused and the JADs exhibit complex structures [Fig. 12(c)]. Correspondingly, if both electrons leave with small energies, we observe correlated angular emission patterns, an example of which can be seen in panel (a).

The JADs shown in Fig. 12 are accurate with respect to the angular momentum expansion to the level of ∼10%. Convergence with R_c depends on the final electron energies. In Fig. 13 we present cuts through JADs of Fig. 12 at $\theta_2 = 0$. If both energies are large, then neither the exact nuclear potential shape nor the postcollision interactions are relevant, and convergence is achieved with $R_c = 30$ a.u. [Fig. 13(b)]. However, if at least one of the electrons energies is small, then electrons may interact with the nucleus over long times and convergence with R_c could only be achieved to the level of qualitative agreement. The overall distribution does not change completely but some qualitative features are still in flux.

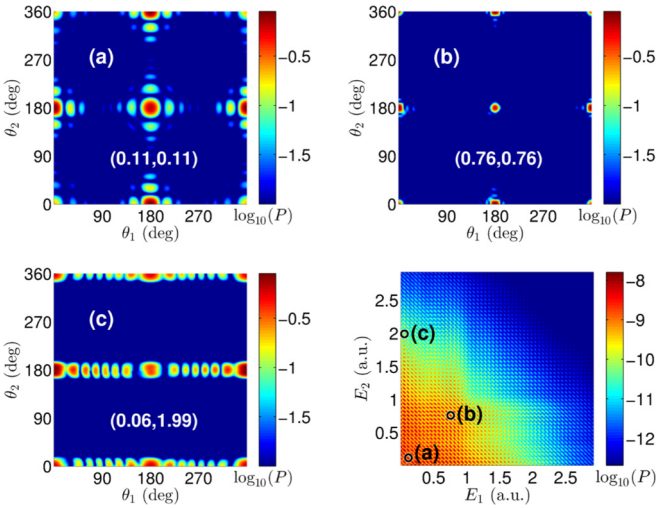

FIG. 12. JADs for wavelength 780 nm and intensity $I = 2 \times 10^{14}$ W/cm^2. Panels (a)–(c) correspond to the energies marked in the $P(E_1, E_2)$ distribution, bottom right panel. Plots are normalized to $\max_{E_1,E_2}[P(E_1, E_2)] = 1$.

For example, at the low emission energies $E_1 = E_2 = 0.11$ [Fig. 13(a)], the dominant emission direction changes from back-to-back to side-by-side when increasing $R_c = 20$ a.u. to $R_c = 25$ a.u. In (c) local minima appear along the polarization axis with $R_c = 30$ a.u.

Clearly, larger R_c are required for convergence at low energies. The present implementation of the method renders such calculations impractical with reasonable computational resources. Also, while for 2×10^{14} W/cm^2 computations with

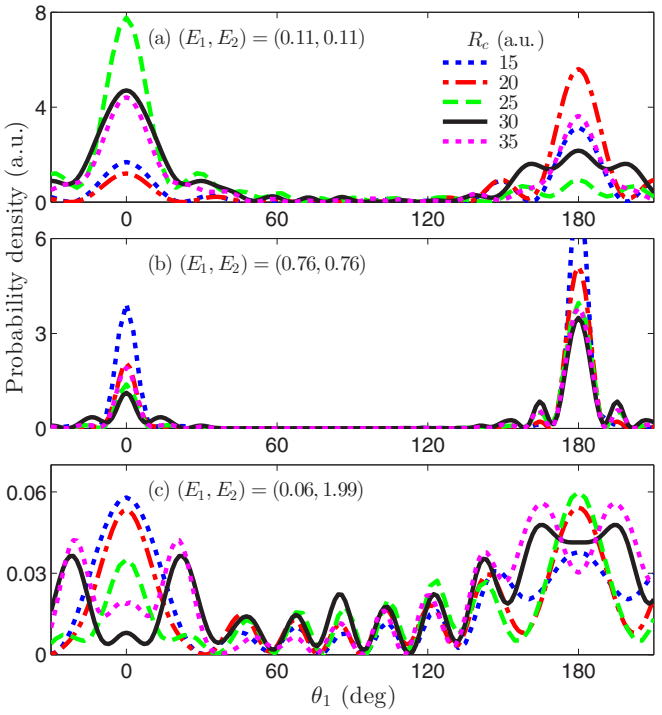

FIG. 13. Cuts through JADs of Fig. 12 at $\theta_2 = 0$ for various values of R_c. At low energies convergence is only qualitative; see (a) and (c). At high energies the angular distribution stabilizes at $R_c = 30$ a.u.; see (b).

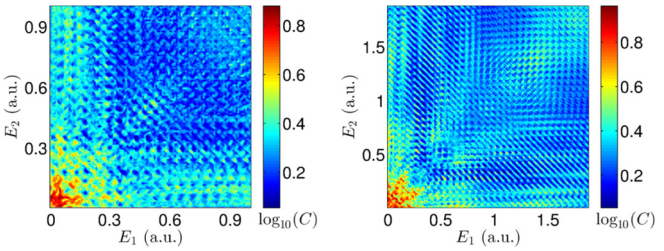

FIG. 14. Angular correlation C as a function of photoelectron energies for intensities 1.6×10^{14} W/cm^2 (left) and 2.0×10^{14} W/cm^2 (right). Computations with $R_c = 30$.

$R_c = 35$ a.u. were still accomplishable, at higher intensities the increasing demand on angular momenta is prohibitive and only computations with up to $R_c = 30$a.u. were practical.

D. Angular correlations

As for XUV DI we compute the angular correlation by Eq. (48) and find it to follow the DI-ATI structure, although not as clearly as in Fig. 6 (see Fig. 14). In addition, at IR wavelength we find maxima at small electron escape energies $E_{1,2} \lesssim 0.2$ a.u. Strong correlation at low energies is to be expected as the electrons interact over longer times before leaving the vicinity of the nucleus.

E. Correlated momentum distribution

Measurements of differential double-emission spectra at IR wavelength were reported in Ref. [13] for $I > 10^{15}$ W/cm^2 and at the somewhat lower intensity of $I = 4.5 \times 10^{14}$ W/cm^2 in Ref. [12]. In Ref. [12] a "fingerlike" structure was found in the photoelectron momentum distribution for side-by-side momenta on the polarization axis $\theta_1 = \theta_2 = 0$ and $\theta_1 = \theta_2 = \pi$. The structure is manifest at energies $>2U_p$, where it shows a minimum at $E_1 = E_2$ and emission maxima off the energy diagonal. It is attributed to electron-impact ionization with backscattering at the nucleus upon recollision, analogous to the recoil peak appearing in field-free ionization by a scattering electron [73]. Similar structures were seen in a $1 + 1$-dimensional model calculation [72].

The laser intensities used in Ref. [12] are just beyond the limitations of the present implementation of tSurff. At wavelength 780 nm and the somewhat lower intensity of $I = 3 \times 10^{14}$ W/cm^2 recolliding electrons can still directly ionize the parent ion, the DI mechanism proposed in Ref. [73] still functions, and one expects similar structures as reported in Ref. [12]. Figure 15 shows that this is indeed the case. In particular, we reproduce the minimum that appears along the diagonal of equal momenta above energies of $2U_p$. Due to the sensitivity of angle-resolved observables to R_c, especially for side-by-side emission, we expect details of our result to change for $R_c > 30$.

F. Convergence with spatial discretization

The most important spatial convergence parameter is the number of partial waves in Eq. (31). We illustrate this for fixed tSurff radius $R_c = 20$.

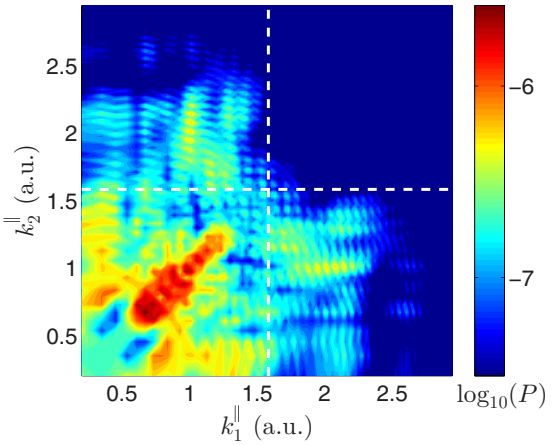

FIG. 15. Correlated side-by-side emission for DI at 780 nm, $I = 3 \times 10^{14}$ W/cm^2, for momenta parallel to the polarization axis. Computation with $R_c = 30$a.u. Dashed lines mark $2U_p$, beyond which "fingerlike" structures appear similar as observed in experiment [12].

With a linearly polarized pulses, the $M = 0$ magnetic quantum number of the He ground state is conserved such that $m_1 = -m_2 =: m$. The population of the m components of Ψ changes only by electron collisions and we found rapid convergence to within our desired precisions at values $m \lesssim 4$.

In contrast, l_1 and l_2 are directly populated by the laser interaction. In the perturbative regime, angular momenta remain small overall, and no particular constraints beyond a simple square $l_1,l_2 \leqslant l_{\max}$ were applied. Also, as overall problem sizes remain comparatively small in the perturbative regime, we made no attempt to rearrange the partial waves into eigenspaces of total angular momentum.

In the nonperturbative regime partial waves reach large l_1,l_2, however, mostly in an L-shaped area of the l_1-l_2-plane. In Fig. 16 we show the peak partial wave populations of the $m = 0$ component of $\Psi(t)$,

$$\rho_{\text{peak}}(l_1,l_2) := \max_t \left\| \langle Y^0_{l_1} Y^0_{l_2} | \Psi(t) \rangle \right\|^2, \tag{53}$$

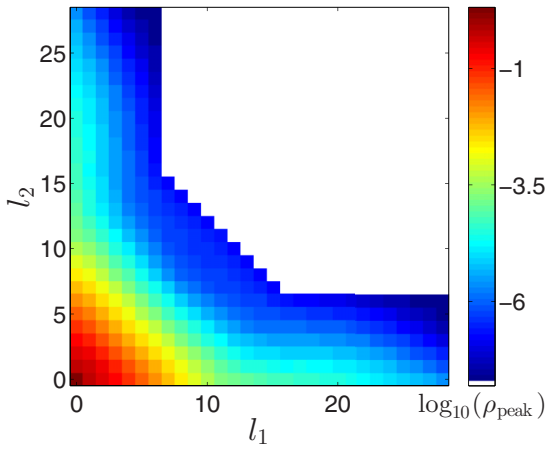

FIG. 16. Peak partial wave populations $\rho_{\text{peak}}(l_1,l_2)$ for a pulse with $\lambda = 780$ nm, $n = 4$, and $I = 2 \times 10^{14}$ W/cm^2.

as reached at any time during the interaction with a four-cycle laser pulse with $\lambda = 780$ nm and $I = 2 \times 10^{14}$ W/cm^2. Similar patterns are found for larger m. Based on this observation, we selected the (l_1,l_2) from an L-shaped region adjusted by inspecting the populations $\rho_{\text{peak}}(l_1,l_2)$ at the borders. Comparing calculations with 551, 639, and 737 partial waves, we find the JADs converged to $<10\%$ almost everywhere. We observed larger differences $\lesssim 30\%$ only near back-to-back and side-by-side emission.

Convergence of the radial expansion is achieved quite easily: For $R_c = 20$a.u. typically four radial sections $r_i^{(n_i)} - r_i^{(n_i-1)} = 5$a.u. were used with degree 11 polynomials at the first element, degree 7 up to $r_i^{(4)} = 20$a.u., and exponentially damped polynomials of maximal degree 19 for absorption in the last section; cf. Eq. (34). The higher degree in the first element accelerates convergence of the two-electron bound state. Such a discretization gives JADs which are radially converged within the accuracies discussed here.

It may be possible to further reduce the radial basis by making the discretization of each $[r_1^{(n_1-1)},r_1^{(n_1)}] \times [r_2^{(n_2-1)},r_2^{(n_2)}]$ patch dependent on its position. For example, at large r_1 and small r_2, the solution in r_2 direction will resemble the lowest ionic bound states which can be parametrized by very few functions. Such constraints were not explored here, but may be useful for further pushing the limits of the calculations.

VII. SUMMARY AND OUTLOOK

We have presented calculations of laser DI of the helium atom in a wide range of intensities and wavelengths. Both XUV and near-IR wavelengths were covered. For the majority of our results we can provide well-founded accuracy estimates.

Our calculations reproduce key literature results at XUV wavelength. As a challenging example we have chosen XUV two-photon DI, where we reproduce available literature results. In the most disputed region near the single-photon ionization threshold we agree with Refs. [9,28,29].

At the IR wavelength of 780 nm we computed *ab initio* the double-to-single-ionization ratio of He. Results conform with experiment and with a numerical recollision model [70], although convergence indicates that Ref. [70] may somewhat overestimate the ratio. We were also able to present differential DI spectra at this wavelength. There are few theoretical results available in the literature for comparison. We qualitatively confirm a two-color XUV-IR result [36] but find notable quantitative deviations. We could extend an observation about a pronounced cutoff in the shared energy momentum spectra reported for $\lambda = 390$ nm in Ref. [34] to 780 nm.

Experiments with He at IR wavelength are mostly performed at higher intensities for reaching sufficient count rates, where we could not reach convergence in the differential spectra with the present implementation. At an intensity slightly below the experimental one, we qualitatively reproduce the correlations observed in doubly differential momentum spectra [12].

All our results are derived from fully differential spectra. Naturally, integrated quantities converge more quickly. In the XUV regime, satisfactory convergence could be obtained for all observables considered. At IR, the double-to-single ratios are accurate to within 20% for the four-cycle pulses

used in the simulations up to intensities 3.5×10^{14} W/cm^2. Energy differential spectra have typical relative errors of $\lesssim$30%, which are exceeded only in limited regions of the E_1E_2 plane. Angle-resolved quantities are most sensitive to our discretization and for IR the corresponding spectra should only be considered as qualitative results when postcollision interactions come into play.

Importantly, calculations presented here are on only moderate computational scale by present-day standards. At XUV wavelength, a maximum of 16 cores on a single computer node were used. The largest calculation at IR wavelength was performed on 128 cores distributed over 8 compute nodes. This should be contrasted with the use of very large scale computer facilities employed for Refs. [9,28,34,36,48,52].

This advancement of possibilities is brought about by the tSurff method, whose potential and limitations we laid out in some detail here. Its main advantage—the numerical simulation on only a small spatial domain—also entails its main shortcoming in the present implementation, namely the inability to reproduce postcollision interactions that occur outside the simulation domain. Fortunately, for a great many of observables and final momenta, postcollision interaction is of secondary importance.

There is a range of possible improvements of the approach. On the one hand, this concerns algorithms and discretization methods. Because we could recently demonstrate that FE-DVR methods are applicable for tSurff [57], replacing the present finite-element discretization with FE-DVR may allow significant reduction of the floating operations count and improve scalability to massive parallel computations. Another algorithmic improvement is to exploit the low multipole order of the electron repulsion at larger distances and the interdependence of radial and angular discretization. On the other hand, as has been indicated in Sec. II B, one may extend tSurff theory by using analytic models for reducing the problems due to the truncation of the potentials at R_c.

By implementing even only part of these measures, full convergence of the differential information at the present parameters and access to more demanding situations such as elliptically polarized IR pulses, DI of multielectron systems (see [41]), or breakup of non-Coulombic systems and systems with reduced symmetry appear realistic.

We conclude with pointing out that an implementation of tSurff method in its scalar single-electron version has been made available as a public-domain code TRECX [74]. Publication of the MPI parallel and two-electron features in the same framework is planned for the near future.

ACKNOWLEDGMENTS

The authors acknowledge financial support by the excellence cluster "Munich Center for Advanced Photonics (MAP)" and by the Austrian Science Foundation Project ViCoM (Grant No. F41). We are grateful to Stefan Nagele for extensive support in detailed comparisons with the TU Wien group's data.

APPENDIX A: MATRIX ELEMENTS $\langle\chi_{\vec{k}}|[H_V,\Theta]|\psi\rangle$

For the commutator matrix element appearing in Eqs. (20), (22), and (12) we express $[H_V,\Theta]$ in polar coordinates for a z-polarized pulse,

$$\left[-\frac{\Delta}{2} - i\vec{A}\cdot\vec{\nabla},\Theta\right] = -\frac{1}{2}\delta(r-R_c)\partial_r - \left(\frac{1}{2}\frac{1}{r^2}\partial_r r^2 + iA_z\cos\theta\right)\delta(r-R_c). \tag{A1}$$

Expanding the plane wave into spherical Bessel functions j_l, the Volkov wave becomes

$$\chi_{\vec{k}}(\vec{r},t) = \frac{e^{-i\Phi(\vec{k},t)}}{\sqrt{\pi/2}}\sum_{l,m} i^l j_l(kr)Y_l^m(\Omega_r)Y_l^{m*}(\Omega_k). \tag{A2}$$

With this, the commutator matrix element is

$$\langle\chi_{\vec{k}}(t)|\left[-\frac{\Delta}{2} - i\vec{A}\cdot\vec{\nabla},\Theta\right]|\psi(t)\rangle = \frac{e^{i\Phi(\vec{k},t)}}{\sqrt{\pi/2}}R_c^2\sum_{l,m}(-i)^l Y_l^m(\Omega_k)(J_{lm} - iA_z K_{lm}), \tag{A3}$$

with the usual flux for the lm partial wave,

$$J_{lm} := \tfrac{1}{2}j_l'(kR_c)R_{lm}(R_c,t) - \tfrac{1}{2}j_l(kR_c)R_{lm}'(R_c,t), \tag{A4}$$

and the correction term for the dipole field,

$$K_{lm} := \sum_{s=\pm1}\left\langle Y_l^m\middle|\cos\theta\middle|Y_{l+s}^m\right\rangle j_l(kR_c)R_{l+s,m}(R_c,t). \tag{A5}$$

APPENDIX B: RYDBERG STATE AVERAGING

Rydberg states extending beyond the tSurff radius R_c lead to artificial oscillating contributions in the photoelectron spectrum. Assume that a hydrogenlike Rydberg state ϕ_n with energy $E_n < 0$ and angular quantum number $l = n-1$ is populated at some time T_0 after the end of the pulse. Its contribution to the tSurff spectrum,

$$b_n(k,T) \sim \langle e^{i\vec{k}\vec{r}}|\Theta|\phi_n\rangle \sim \frac{\sin(kR_c)}{k^2}, \tag{B1}$$

oscillates at constant amplitude,

$$b_n(k,T') = b_n(k,T)e^{i(T'-T)(E_n-k^2/2)}. \tag{B2}$$

Averaging $b(k,T')$ over a time interval ΔT,

$$\frac{1}{\Delta T}\int_T^{T+\Delta T} b_n(k,T')dT' \sim \frac{b_n(k,T_0)}{\Delta T(E_n-k^2/2)}. \tag{B3}$$

suppresses the artifact. In the spectra the decrease squares $\sim(\Delta T)^{-2}$. True outgoing flux is not affected if averaging starts at times T, where all relevant flux has passed the surface. Figure 17 illustrates the suppression for the two-particle case.

APPENDIX C: RADIAL BASIS AND INVERSE OVERLAP

The following was applied to the two radial axes of the two-electron system (31) and the radial axis of the single-electron system (32). We use a high-degree finite-element discretization whose construction is described in Ref. [51]. We divide the axis into N elements $[r_{n-1},r_n]$, $n = 1,\ldots,N$. On each element we

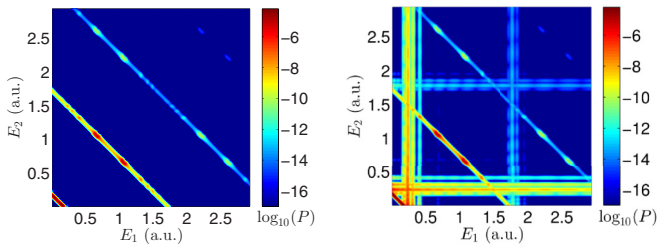

FIG. 17. (Left) Energy probability distribution $P(E_1,E_2)$ for a $n = 120$ cycle pulse with photon energy $\hbar\omega = 42$ eV and peak intensity $I = 10^{13}$ W/cm^2 using a $\cos^8$ envelope and averaging time $\Delta T = 1$ ps. (Right) Without averaging.

have p_n linearly independent functions $\{f_i^{(n)}, i = 1,\ldots,p_n\}$ satisfying

$$f_k^{(n)}(r_{n-1}) = 0 = f_k^{(n)}(r_n),$$
$$\text{except } f_1^{(n)}(r_{n-1}) = 1 = f_{p_n}^{(n)}(r_n). \tag{C1}$$

With these conditions, the overlap matrix on each finite element $S_{ij}^{(n)} = \langle f_i^{(n)}|f_j^{(n)}\rangle$ can be transformed such that its diagonal except for the two off-diagonal elements $\langle f_1^{(n)}|f_{p_n}^{(n)}\rangle \neq 0$. The end-elements $n = 0$ and $n = N$ may have modified constraints for the purpose of implementing the boundary conditions. The radial wave function is then given by $\psi(r,t) = \sum_{n=1}^{N}\sum_{k=1}^{p_n} f_k^{(n)}(r)c_k^{(n)}(t)$. Continuity across element boundaries is assured by demanding $c_{p_{n-1}}^{(n-1)} = c_1^{(n)}$ for $n \geqslant 2$. The application of an operator matrix thus amounts to the blockwise application to each finite element and then enforcing continuity, which is done by averaging the corresponding coefficients,

$$\left(c_{p_{n-1}}^{(n-1)}, c_1^{(n)}\right) \mapsto \left(\frac{c_{p_{n-1}}^{(n-1)} + c_1^{(n)}}{2}, \frac{c_{p_{n-1}}^{(n-1)} + c_1^{(n)}}{2}\right). \tag{C2}$$

This map can be implemented by a projector $\widehat{Q}$ as follows. First, identify the wave functions with the coefficient vector $\psi \leftrightarrow \vec{c} \in \mathbb{C}^d$, where $d = \sum_{n=1}^{N} p_n$ gives the overall number of coefficients. For

$$\vec{n}^T = \left(0,\ldots,0,-\frac{1}{\sqrt{2}},0,\ldots,0,\frac{1}{\sqrt{2}},0,\ldots,0\right) \in \mathbb{R}^d, \tag{C3}$$

the map $\widehat{\mathbb{1}} - \vec{n}\otimes\vec{n}^{\mathrm{T}}$ realizes the above averaging for the element boundary at r_n if the two nonzero coefficients in $\vec{n}$ are at the positions of $c_{p_{n-1}}^{(n-1)}$ and $c_1^{(n)}$ in the overall coefficient vector $\vec{c}$. The full projector is then given by $\widehat{Q} = \widehat{\mathbb{1}} - \sum_n \vec{n}\otimes\vec{n}^{\mathrm{T}}$, which can be written as

$$\widehat{Q} = \widehat{\mathbb{1}} - \widehat{R}\widehat{R}^{\mathrm{T}}, \tag{C4}$$

with the $d \times (N-1)$ matrix

$$\widehat{R} = (\vec{2},\ldots,\vec{n},\ldots,\vec{N}). \tag{C5}$$

The application of the inverse overlap requires extra attention as it must be constrained to the subspace of continuous vectors $\widehat{Q}\vec{c}$: It is the inverse in the sense $(\widehat{Q}\widehat{S}\widehat{Q})^{-1}(\widehat{Q}\widehat{S}\widehat{Q}) = (\widehat{Q}\widehat{S}\widehat{Q})(\widehat{Q}\widehat{S}\widehat{Q})^{-1} = \widehat{Q}$. The formula used is a variation of the Woodbury matrix identity. It takes the form

$$(\widehat{Q}\widehat{S}\widehat{Q})^{-1} = [\widehat{\mathbb{1}} - \widehat{S}^{-1}\widehat{R}(\widehat{R}^{\mathrm{T}}\widehat{S}^{-1}\widehat{R})^{-1}\widehat{R}^{\mathrm{T}}]\widehat{S}^{-1}, \tag{C6}$$

where $\widehat{S}^{-1}$ is the blockwise inverse without the constraint $\widehat{Q}$. This reduces the application of inverse of $\widehat{Q}\widehat{S}\widehat{Q}$ to the application of N near diagonal blockwise inverse $[\widehat{S}^{(n)}]^{-1}$ (operations count $\propto Np$) and the correction by $\widehat{S}^{-1}\widehat{R}(\widehat{R}^{\mathrm{T}}\widehat{S}^{-1}\widehat{R})^{-1}$ with operations count $\sim dN + N^2$.

In two-particle calculations two one-particle inverses need to be applied in sequence because of the tensor product form of the overlap $\widehat{S} = \widehat{S}_1 \otimes \widehat{S}_2$.

APPENDIX D: MULTIPOLE OPERATORS

In the multipole expansion of the electron-electron interaction (Sec. III D) appear multipole matrices $\widehat{V}^{(\lambda)}$. For fixed angular momentum indices (omitted here) and fixed finite element (n_1,n_2), and inserting the radial basis [Eq. (34)], these are given by

$$\widehat{V}^{(\lambda,n_1n_2)}_{p_1'p_2',p_1p_2} = \int dr_1 \int dr_2 \frac{\min(q_i,q_j)^\lambda}{\max(q_i,q_j)^{\lambda+1}} \times f_{p_1'}^{(n_1)}(r_1) f_{p_2'}^{(n_2)}(r_2) f_{p_1}^{(n_1)}(r_1) f_{p_2}^{(n_2)}(r_2). \tag{D1}$$

If the maximal degree of the polynomial expansion is $P-1$, then the product polynomials

$$f_{p_i'}^{(n_i)}(r_i) f_{p_i}^{(n_i)}(r_i) =: F_{K_i}^{(n_i)}(r_i), \quad i = 1,2,$$

have maximal degree $2P-2$, with at most $2P-1$ linearly independent functions $F_{K_i}^{(n_i)}(r_i)$. We rearrange the indices $p_1'p_2', p_1p_2$ into $K_1 = (p_1'p_1)$ and $K_2 = (p_2'p_2)$ and consider $\widehat{V}^{(\lambda)}_{p_1'p_2',p_1p_2}$ as a two-index $P^2 \times P^2$ matrix $\widehat{W}^{(\lambda)}_{K_1,K_2}$. This matrix has a maximal rank of $R := 2P-1$ and, in a suitable representation, it reduces to a $R \times R$ matrix $\widehat{D}_{ij}^{(\lambda)}$. One such representation is with respect to R-point Gaussian quadrature grids: $\{q_i^{(n_1)}, w_i^{(n_1)}\}_{i=1,\ldots,R}$ on the the interval $[r_1^{(n_1-1)}, r_1^{(n_1)}]$ and $\{q_j^{(n_2)}, w_j^{(n_2)}\}_{j=1,\ldots,R}$ on $[r_2^{(n_2-1)}, r_2^{(n_2)}]$, where $w_i^{(n_1)}$ and $w_j^{(n_2)}$ are the associated quadrature weights. For these grids we have

$$\widehat{D}_{ij}^{(\lambda)} = \sum_{K_1,K_2} F_{K_1}^{(n_1)}\left(q_i^{(n_1)}\right) \widehat{W}^{(\lambda)}_{K_1,K_2} F_{K_2}^{(n_2)}\left(q_j^{(n_2)}\right). \tag{D2}$$

The transformation from the P^2 coefficients to the $R < P^2$ coefficients can be done separately for each coordinate; i.e., it has tensor product structure and operations count $RP(R+P) \propto P^3$. It is given by $\widehat{T}^{(n_1)} \otimes \widehat{T}^{(n_2)}$, with

$$\widehat{T}^{(n_\alpha)}_{i_\alpha,p_\alpha} = \sqrt{w_{i_\alpha}^{(n_\alpha)}}\, f_{p_\alpha}^{(n_\alpha)}\left(q_{i_\alpha}^{(n_\alpha)}\right), \quad \alpha = 1,2. \tag{D3}$$

Thus, the application of $\widehat{V}^{(\lambda)}_{p_1'p_2',p_1p_2}$ amounts to a transformation to the reduced representation with R coefficients, the coefficientwise multiplication with $\widehat{D}_{ij}^{(\lambda)}$ (operations count R^2), and the back-transformation to the representation with P^2 coefficients,

$$\widehat{V}^{(\lambda,n_1n_2)}_{p_1'p_2',p_1p_2} = \sum_{ij} \left(\widehat{T}^{(n_1)}_{i,p_1'} \otimes \widehat{T}^{(n_2)}_{j,p_2'}\right)^{\mathrm{T}} \widehat{D}_{ij}^{(\lambda)} \left(\widehat{T}^{(n_1)}_{i,p_1} \otimes \widehat{T}^{(n_2)}_{j,p_2}\right); \tag{D4}$$

compare Eq. (39).

The integrals $\widehat{W}^{(\lambda)}_{K_1,K_2}$ for generating the correct $\widehat{D}^{(\lambda)}_{ij}$ (D2) need to be evaluated only once during setup. This step must not be bypassed by using $\min(q_i,q_j)^\lambda/\max(q_i,q_j)^{\lambda+1}$, as this potential is not suitable for direct integration with a Gaussian quadrature on the product grid $q_i q_j$.

In practice, we found that the quadratures do not need to be done exactly. Minor quadrature errors introduced by a Gaussian quadrature grid with only P or even fewer points are acceptable, which further reduces the operations count.

It is obvious from the derivation that the same procedure can be applied for any two-dimensional multiplicative potential and gives the exact matrix elements for a given polynomial product basis. It is most useful for potentials that have points of nonanalyticity, such as the Coulomb potential. For potentials with a convergent Taylor series, Gaussian quadrature can be usually applied directly.

APPENDIX E: IRECS

ECS is the coordinate rotation into the lower complex plane, defined by

$$r \mapsto r_\theta = \begin{cases} r & r \leqslant R_0, \\ e^{i\theta}(r - R_0) + R_0 & r > R_0, \end{cases} \tag{E1}$$

with the scaling angle $\theta > 0$. We can choose any $R_0 > R_c$. We let the scaling radius R_0 fall onto an element boundary of the finite-element discretization of the radial axis. Following the specifications in Ref. [51], ECS can then be realized by introducing an explicit discontinuity in the basis functions f_i at the scaling radius R_0:

$$f_i^{(\theta)}(r) = \begin{cases} f_i(r) & r < R_0, \\ e^{i\theta/2} f_i(r) & r > R_0. \end{cases} \tag{E2}$$

This translates into scaled matrices in the discretized TDSE (36).

The overlap matrix $\widehat{S}_{ij} = \langle f_i | f_j \rangle$ transforms into $\widehat{S}_\theta$ in the scaled region as

$$\widehat{S}_{\theta,ij} = \int dr (e^{i\theta/2} f_i)(r)(e^{i\theta/2} f_j)(r) = e^{i\theta}\widehat{S}_{ij}. \tag{E3}$$

Note that the left-hand side $e^{i\theta/2}$ does not get complex conjugated, as explained in Ref. [51]. The various terms in the Hamiltonian matrix $\widehat{H}$ transform accordingly. Potential terms are evaluated at complex values, which requires the analytic continuation of these potentials,

$$\widehat{V}_{\theta,ij} = \left\langle f_i^{(\theta)} \middle| V(r_\theta) \middle| f_j^{(\theta)} \right\rangle. \tag{E4}$$

The same principle applies for the evaluation of derivatives, observing that $\partial/\partial(e^{i\theta} r) = e^{-i\theta}\partial/\partial r$. For example, for elements outside R_0, the complex scaled matrix for the second derivative is

$$-\left\langle \frac{\partial f_i^{(\theta)}}{\partial e^{i\theta} r} \middle| \frac{\partial f_i^{(\theta)}}{\partial e^{i\theta} r} \right\rangle = -e^{-i\theta} \left\langle \frac{\partial f_i}{\partial r} \middle| \frac{\partial f_j}{\partial r} \right\rangle. \tag{E5}$$

The implementation of complex scaling thus amounts to simple multiplications of the matrices with factors of $e^{i\theta}$ and evaluation of potential terms at complex values.

This applies to both standard ECS and infinite-range ECS. For the implementation of irECS, basis functions on the last element extend to infinity and integration needs to be performed over the complete range [51].

[1] B. Walker, B. Sheehy, L. F. DiMauro, P. Agostini, K. J. Schafer, and K. C. Kulander, Precision Measurement of Strong Field Double Ionization of Helium, Phys. Rev. Lett. **73**, 1227 (1994).

[2] V. L. B. de Jesus, B. Feuerstein, K. Zrost, D. Fischer, A. Rudenko, F. Afaneh, C. D. Schröter, R. Moshammer, and J. Ullrich, Atomic structure dependence of nonsequential double ionization of He, Ne and Ar in strong laser pulses, J. Phys. B **37**, L161 (2004).

[3] W. Becker and H. Rottke, Many-electron strong-field physics, Contemp. Phys. **49**, 199 (2008).

[4] P. B. Corkum, Plasma Perspective on Strong Field Multiphoton Ionization, Phys. Rev. Lett. **71**, 1994 (1993).

[5] S. L. Haan, L. Breen, A. Karim, and J. H. Eberly, Variable Time Lag and Backward Ejection in Full-Dimensional Analysis of Strong-Field Double Ionization, Phys. Rev. Lett. **97**, 103008 (2006).

[6] T. Shaaran, M. T. Nygren, and C. Figueira de Morisson Faria, Laser-induced nonsequential double ionization at and above the recollision-excitation-tunneling threshold, Phys. Rev. A **81**, 063413 (2010).

[7] A. Emmanouilidou, Prevalence of different double ionization pathways and traces of three-body interactions in strongly driven helium, Phys. Rev. A **83**, 023403 (2011).

[8] L. A. A. Nikolopoulos and P. Lambropoulos, Time-dependent theory of double ionization of helium under xuv radiation, J. Phys. B **40**, 1347 (2007).

[9] J. Feist, S. Nagele, R. Pazourek, E. Persson, B. I. Schneider, L. A. Collins, and J. Burgdörfer, Nonsequential two-photon double ionization of helium, Phys. Rev. A **77**, 043420 (2008).

[10] J. Ullrich, R. Moshammer, A. Dorn, R. Dörner, L. P. H. Schmidt, and H. Schmidt-Böcking, Recoil-ion and electron momentum spectroscopy: Reaction-microscopes, Rep. Prog. Phys. **66**, 1463 (2003).

[11] L. Avaldi and A. Huetz, Photodouble ionization and the dynamics of electron pairs in the continuum, J. Phys. B **38**, S861 (2005).

[12] A. Staudte, C. Ruiz, M. Schöffler, S. Schössler, D. Zeidler, T. Weber, M. Meckel, D. M. Villeneuve, P. B. Corkum, A. Becker, and R. Dörner, Binary and Recoil Collisions in Strong Field Double Ionization of Helium, Phys. Rev. Lett. **99**, 263002 (2007).

[13] A. Rudenko, V. L. B. de Jesus, T. Ergler, K. Zrost, B. Feuerstein, C. D. Schröter, R. Moshammer, and J. Ullrich, Correlated Two-Electron Momentum Spectra for Strong-Field Nonsequential Double Ionization of He at 800 nm, Phys. Rev. Lett. **99**, 263003 (2007).

[14] A. Rudenko *et al.*, Recoil-Ion Momentum Distributions for Two-Photon Double Ionization of He and Ne by 44 ev Free-Electron Laser Radiation, Phys. Rev. Lett. **101**, 073003 (2008).
[15] A. Fleischer, H. J. Wörner, L. Arissian, L. R. Liu, M. Meckel, A. Rippert, R. Dörner, D. M. Villeneuve, P. B. Corkum, and A. Staudte, Probing Angular Correlations in Sequential Double Ionization, Phys. Rev. Lett. **107**, 113003 (2011).
[16] M. A. Stevenson and B. Lohmann, Fully differential cross-section measurements for electron-impact ionization of argon over the complete in-plane angular range, Phys. Rev. A **77**, 032708 (2008).
[17] A. N. Pfeiffer, C. Cirelli, M. Smolarski, R. Dörner, and U. Keller, Timing the release in sequential double ionization, Nat. Phys. **7**, 428 (2011).
[18] B. Bergues, M. Kübel, N. G. Johnson, B. Fischer, N. Camus, K. J. Betsch, O. Herrwerth, A. Senftleben, A. M. Sayler, T. Rathje, T. Pfeifer, I. Ben-Itzhak, R. R. Jones, G. G. Paulus, F. Krausz, R. Moshammer, J. Ullrich, and M. F. Kling, Attosecond tracing of correlated electron-emission in non-sequential double ionization, Nat. Commun. **3**, 813 (2012).
[19] K. Henrichs, M. Waitz, F. Trinter, H. Kim, A. Menssen, H. Gassert, H. Sann, T. Jahnke, J. Wu, M. Pitzer, M. Richter, M. S. Schöffler, M. Kunitski, and R. Dörner, Observation of Electron Energy Discretization in Strong Field Double Ionization, Phys. Rev. Lett. **111**, 113003 (2013).
[20] Y. Liu, L. Fu, D. Ye, J. Liu, M. Li, C. Wu, Q. Gong, R. Moshammer, and J. Ullrich, Strong-Field Double Ionization Through Sequential Release from Double Excitation with Subsequent Coulomb Scattering, Phys. Rev. Lett. **112**, 013003 (2014).
[21] A. S. Kheifets and I. A. Ivanov, Convergent close-coupling calculations of two-photon double ionization of helium, J. Phys. B **39**, 1731 (2006).
[22] D. A. Horner, F. Morales, T. N. Rescigno, F. Martín, and C. W. McCurdy, Two-photon double ionization of helium above and below the threshold for sequential ionization, Phys. Rev. A **76**, 030701 (2007).
[23] L. Malegat, H. Bachau, A. Hamido, and B. Piraux, Analysing a two-electron wavepacket by semiclassically propagating its fourier components in space, J. Phys. B **43**, 245601 (2010).
[24] L. Argenti, R. Pazourek, J. Feist, S. Nagele, M. Liertzer, E. Persson, J. Burgdorfer, and E. Lindroth, Photoionization of helium by attosecond pulses: Extraction of spectra from correlated wave functions, Phys. Rev. A **87**, 053405 (2013).
[25] L. Feng and H. W. van der Hart, Two-photon double ionization of he, J. Phys. B **36**, L1 (2003).
[26] P. G. Burke, P. Francken, and C. J. Joachain, R -matrix-floquet theory of multiphoton processes, J. Phys. B **24**, 761 (1991).
[27] B. I. Schneider, L. A. Collins, and S. X. Hu, Parallel solver for the time-dependent linear and nonlinear schrödinger equation, Phys. Rev. E **73**, 036708 (2006).
[28] A. Palacios, D. A. Horner, T. N. Rescigno, and C. W. McCurdy, Two-photon double ionization of the helium atom by ultrashort pulses, J. Phys. B **43**, 194003 (2010).
[29] R. Nepstad, T. Birkeland, and M. Førre, Numerical study of two-photon ionization of helium using an *ab initio* numerical framework, Phys. Rev. A **81**, 063402 (2010).
[30] Z. Zhang, L. Y. Peng, M. H. Xu, A. F. Starace, T. Morishita, and Q. Gong, Two-photon double ionization of helium: Evolution of the joint angular distribution with photon energy and two-electron energy sharing, Phys. Rev. A **84**, 043409 (2011).
[31] W. C. Jiang, L. Y. Peng, W. H. Xiong, and Q. Gong, Comparison study of electron correlation in one-photon and two-photon double ionization of helium, Phys. Rev. A **88**, 023410 (2013).
[32] A. Liu and U. Thumm, Laser-assisted xuv few-photon double ionization of helium: Joint angular distributions, Phys. Rev. A **89**, 063423 (2014).
[33] J. S. Parker, B. J. S. Doherty, K. J. Meharg, and K. T. Taylor, Time delay between singly and doubly ionizing wavepackets in laser-driven helium, J. Phys. B **36**, L393 (2003).
[34] J. S. Parker, B. J. S. Doherty, K. T. Taylor, K. D. Schultz, C. I. Blaga, and L. F. DiMauro, High-Energy Cutoff in the Spectrum of Strong-Field Nonsequential Double Ionization, Phys. Rev. Lett. **96**, 133001 (2006).
[35] A. Emmanouilidou, J. S. Parker, L. R. Moore, and K. T. Taylor, Direct versus delayed pathways in strong-field non-sequential double ionization, New J. Phys. **13**, 043001 (2011).
[36] S. X. Hu, Boosting Photoabsorption by Attosecond Control of Electron Correlation, Phys. Rev. Lett. **111**, 123003 (2013).
[37] L. Tao and A. Scrinzi, Photo-electron momentum spectra from minimal volumes: the time-dependent surface flux method, New J. Phys. **14**, 013021 (2012).
[38] C. Hofmann, A. S. Landsman, A. Zielinski, C. Cirelli, T. Zimmermann, A. Scrinzi, and U. Keller, Interpreting electron-momentum distributions and nonadiabaticity in strong-field ionization, Phys. Rev. A **90**, 043406 (2014).
[39] A. Karamatskou, S. Pabst, Y.-J. Chen, and R. Santra, Calculation of photoelectron spectra within the time-dependent configuration-interaction singles scheme, Phys. Rev. A **89**, 033415 (2014).
[40] L. Yue and L. B. Madsen, Dissociative ionization of H_2^+ using intense femtosecond xuv laser pulses, Phys. Rev. A **90**, 063408 (2014).
[41] V. P. Majety, A. Zielinski, and A. Scrinzi, Photoionization of few electron systems: a hybrid coupled channels approach, New J. Phys. **17**, 063002 (2015).
[42] V. P. Majety, A. Zielinski, and A. Scrinzi, Mixed gauge in strong laser-matter interaction, J. Phys. B **48**, 025601 (2015).
[43] L. Torlina, F. Morales, J. Kaushal, I. Ivanov, A. Kheifets, A. Zielinski, A. Scrinzi, H. G. Muller, S. Sukiasyan, M. Ivanov, and O. Smirnova, Interpreting attoclock measurements of tunneling times, Nat. Phys. **11**, 503 (2015).
[44] A. Scrinzi, t-surff: fully differential two-electron photo-emission spectra, New J. Phys. **14**, 085008 (2012).
[45] M. S. Pindzola, F. Robicheaux, S. D. Loch, J. C. Berengut, T. Topcu, J. Colgan, M. Foster, D. C. Griffin, C. P. Ballance, D. R. Schultz, T. Minami, N. R. Badnell, M. C. Witthoeft, D. R. Plante, D. M. Mitnik, J. A. Ludlow, and U. Kleiman, The time-dependent close-coupling method for atomic and molecular collision processes, J. Phys. B **40**, R39 (2007).
[46] C. W. McCurdy, M. Baertschy, and T. N. Rescigno, Solving the three-body coulomb breakup problem using exterior complex scaling, J. Phys. B **37**, R137 (2004).
[47] T. Schneider, P. L. Chocian, and J.-M. Rost, Separation and Identification of Dominant Mechanisms in Double Photoionization, Phys. Rev. Lett. **89**, 073002 (2002).
[48] R. Pazourek, J. Feist, S. Nagele, E. Persson, B. I. Schneider, L. A. Collins, and J. Burgdörfer, Universal features in sequential

and nonsequential two-photon double ionization of helium, Phys. Rev. A **83**, 053418 (2011).

[49] O. Smirnova, M. Spanner, and M. Ivanov, Analytical solutions for strong field-driven atomic and molecular one- and two-electron continua and applications to strong-field problems, Phys. Rev. A **77**, 033407 (2008).

[50] A. Zielinski, V. P. Majety, S. Nagele, R. Pazourek, J. Burgdörfer, and A. Scrinzi, Anomalous Fano Profiles in External Fields, Phys. Rev. Lett. **115**, 243001 (2015).

[51] A. Scrinzi, Infinite-range exterior complex scaling as a perfect absorber in time-dependent problems, Phys. Rev. A **81**, 053845 (2010).

[52] J. Feist, S. Nagele, R. Pazourek, E. Persson, B. I. Schneider, L. A. Collins, and J. Burgdörfer, Probing Electron Correlation Via Attosecond Xuv Pulses in the Two-Photon Double Ionization of Helium, Phys. Rev. Lett. **103**, 063002 (2009).

[53] H. F. Trotter, On the product of semi-groups of operators, Proc. Am. Math. Soc. **10**, 545 (1959).

[54] M. Suzuki, Decomposition formulas of exponential operators and lie exponentials with some applications to quantum mechanics and statistical physics, J. Math. Phys. **26**, 601 (1985).

[55] E. Cormier and P. Lambropoulos, Optimal gauge and gauge invariance in non-perturbative time-dependent calculation of above-threshold ionization, J. Phys. B **29**, 1667 (1996).

[56] L. Tao, W. Vanroose, B. Reps, T. N. Rescigno, and C. W. McCurdy, Long-time solution of the time-dependent schrödinger equation for an atom in an electromagnetic field using complex coordinate contours, Phys. Rev. A **80**, 063419 (2009).

[57] M. Weinmüller, M. Weinmüller, J. Rohland, and A. Scrinzi, Perfect absorption in schrödinger-like problems using non-equidistant complex grids, arXiv:1509.04947.

[58] E. S. Smyth, J. S. Parker, and K. Taylor, Numerical integration of the time-dependent schrödinger equation for laser-driven helium, Comput. Phys. Commun. **114**, 1 (1998).

[59] L. Collins, J. Kress, and R. Walker, Excitation and ionization of molecules by a single-mode laser field using a time-dependent approach, Comput. Phys. Commun. **114**, 15 (1998).

[60] R. Grobe, K. Rzazewski, and J. H. Eberly, Measure of electron-electron correlation in atomic physics, J. Phys. B **27**, L503 (1994).

[61] D. Hochstuhl, C. Hinz, and M. Bonitz, Time-dependent multiconfiguration methods for the numerical simulation of photoionization processes of many-electron atoms, The European Physical Journal Special Topics **223**, 177 (2014).

[62] L. Malegat, H. Bachau, B. Piraux, and F. Reynal, A novel estimate of the two-photon double-ionization cross section of helium, J. Phys. B **45**, 175601 (2012).

[63] I. A. Ivanov and A. S. Kheifets, Two-photon double ionization of helium in the region of photon energies 42-50 ev, Phys. Rev. A **75**, 033411 (2007).

[64] E. Foumouo, G. L. Kamta, G. Edah, and B. Piraux, Theory of multiphoton single and double ionization of two-electron atomic systems driven by short-wavelength electric fields: An *ab initio* treatment, Phys. Rev. A **74**, 063409 (2006).

[65] S. X. Hu, J. Colgan, and L. A. Collins, Triple-differential cross-sections for two-photon double ionization of he near threshold, J. Phys. B **38**, L35 (2005).

[66] B. Piraux, J. Bauer, S. Laulan, and H. Bachau, Probing electron-electron correlation with attosecond pulses, Eur. Phys. J. D **26**, 7 (2003).

[67] S. Laulan and H. Bachau, Correlation effects in two-photon single and double ionization of helium, Phys. Rev. A **68**, 013409 (2003).

[68] J. S. Parker, L. R. Moore, K. J. Meharg, D. Dundas, and K. T. Taylor, Double-electron above threshold ionization of helium, J. Phys. B **34**, L69 (2001).

[69] F. Maulbetsch and J. S. Briggs, Selection rules for transitions to two-electron continuum states, J. Phys. B **28**, 551 (1995).

[70] T. Ishikawa, X. M. Tong, and N. Toshima, Double ionization of he in an intense laser field via a rescattering process, Phys. Rev. A **82**, 033411 (2010).

[71] M. Ammosov, N. Delone, and V. Krainov, Tunnel ionization of complex atoms and of atomic ions in an alternating electromagnetic field, Zh. Eksp. Teor. Fiz. **91**, 2008 (1986) [Sov. Phys. JETP **64**, 1191 (1986)].

[72] Q. Liao and P. Lu, Energy correlation in above-threshold nonsequential double ionization at 800 nm, Phys. Rev. A **82**, 021403 (2010).

[73] Z. Chen, Y. Liang, and C. D. Lin, Quantum Theory of Recollisional (e, $2e$) Process in Strong Field Nonsequential Double Ionization of Helium, Phys. Rev. Lett. **104**, 253201 (2010).

[74] The TRECX code (online), available at http://homepages.physik.uni-muenchen.de/~armin.scrinzi/tRecX/.